



National Aeronautics and
Space Administration

TechBriefs



Electronic Components and Circuits



Electronic Systems



Physical Sciences



Materials



Computer Programs



Mechanics



Machinery

Am 2002004141



Fabrication Technology



Mathematics and Information Sciences



Life Sciences

INTRODUCTION

Tech Briefs are short announcements of innovations originating from research and development activities of the National Aeronautics and Space Administration. They emphasize information considered likely to be transferable across industrial, regional, or disciplinary lines and are issued to encourage commercial application.

Availability of NASA Tech Briefs and TSPs

Requests for individual Tech Briefs or for Technical Support Packages (TSPs) announced herein should be addressed to

National Technology Transfer Center

Telephone No. (800) 678-6882 or via World Wide Web at www2.nttc.edu/leads/

Please reference the control numbers appearing at the end of each Tech Brief. Information on NASA's Commercial Technology Team, its documents, and services is also available at the same facility or on the World Wide Web at www.nctn.hq.nasa.gov.

Commercial Technology Offices and Patent Counsels are located at NASA field centers to provide technology-transfer access to industrial users. Inquiries can be made by contacting NASA field centers and program offices listed below.

NASA Field Centers and Program Offices

Ames Research Center

Carolina Blake
(650) 604-1754 or
cblake@mail.arc.nasa.gov

Dryden Flight Research Center

Jenny Baer-Riedhart
(661) 276-3689 or
jenny.baer-riedhart@dfrc.nasa.gov

Goddard Space Flight Center

George Alcorn
(301) 286-5810 or
galcorn@gsfc.nasa.gov

Jet Propulsion Laboratory

Merle McKenzie
(818) 354-2577 or
merle.mckenzie@jpl.nasa.gov

Johnson Space Center

Hank Davis
(281) 483-0474 or
henny.l.davis1@jsc.nasa.gov

John F. Kennedy Space Center

Jim Aliberti
(321) 867-6224 or
Jim.Aliberti-1@ksc.nasa.gov

Langley Research Center

Sam Morello
(757) 864-6005 or
s.a.morello@larc.nasa.gov

Glenn Research Center

Larry Viterna
(216) 433-3484 or
cto@grc.nasa.gov

George C. Marshall Space Flight Center

Sally Little
(256) 544-4266 or
sally.little@msfc.nasa.gov

John C. Stennis Space Center

Kirk Sharp
(228) 688-1929 or
technology@ssc.nasa.gov

NASA Program Offices

At NASA Headquarters there are seven major program offices that develop and oversee technology projects of potential interest to industry:

Carl Ray

Small Business Innovation Research Program (SBIR) & Small Business Technology Transfer Program (STTR)
(202) 358-4652 or
cray@mail.hq.nasa.gov

Dr. Robert Norwood

Office of Commercial Technology
(Code RW)
(202) 358-2320 or
rnorwood@mail.hq.nasa.gov

John Mankins

Office of Space Flight (Code MP)
(202) 358-4659 or
jmankins@mail.hq.nasa.gov

Terry Hertz

Office of Aero-Space Technology
(Code RS)
(202) 358-4636 or
thertz@mail.hq.nasa.gov

Glen Mucklow

Office of Space Sciences
(Code SM)
(202) 358-2235 or
gmucklow@mail.hq.nasa.gov

Roger Crouch

Office of Microgravity Science Applications (Code U)
(202) 358-0689 or
rcrouch@mail.hq.nasa.gov

Granville Paules

Office of Mission to Planet Earth
(Code Y)
(202) 358-0706 or
gpaules@mtpe.hq.nasa.gov



5 Electronic Components and Circuits



13 Electronic Systems



17 Physical Sciences



29 Materials



35 Computer Programs



39 Mechanics



45 Machinery



51 Mathematics and Information Sciences



This document was prepared under the sponsorship of the National Aeronautics and Space Administration. Neither the United States Government nor any person acting on behalf of the United States Government assumes any liability resulting from the use of the information contained in this document, or warrants that such use will be free from privately owned rights.

4

BLANK PAGE



Electronic Components and Circuits

Hardware, Techniques, and Processes

- 7 Ceramic Ribbons as Waveguides at Millimeter Wavelengths
- 8 Micromachined Broad Band Light Sources
- 9 CMOS Image Sensors Capable of Time-Delayed Integration
- 10 Leakage-Preventing Design of Snapshot Photodiode CMOS Imager

Ceramic Ribbons as Waveguides at Millimeter Wavelengths

Very low loss can be obtained in a dominant TM-like mode.

NASA's Jet Propulsion Laboratory,
Pasadena, California

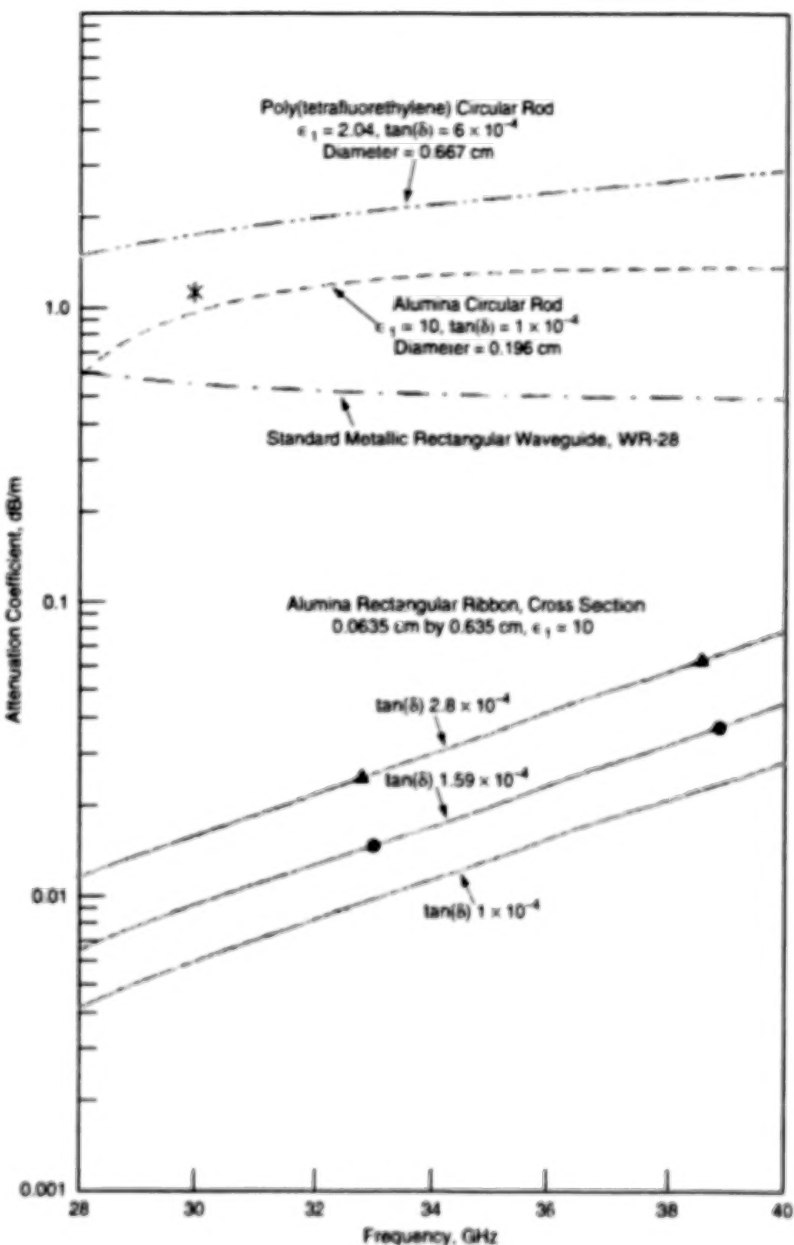
Theoretical calculations verified by experiments have shown that suitably designed ribbons made of alumina can serve as low-loss dielectric waveguides for electromagnetic radiation at frequencies from 30 to 300 GHz. Prior to this development, low-loss waveguides for this frequency range were unknown. The achievable attenuation factor for an alumina-ribbon waveguide is less than 10 dB/km; as such, it is less than a hundredth of that of a typical ceramic dielectric rod waveguide, less than 1/200 of that of a customary metallic waveguide, and less than 1/300 of that of a microstripline at a frequency of 100 GHz.

The exceptionally low loss factor is not achieved primarily, as it has been on some past occasions, through selection of ultra-low-loss dielectric material (since ultra-low-loss material is not obtainable in this frequency range). Instead, it is achieved primarily through selection of a cross-sectional geometry in conjunction with a reasonably low-loss dielectric material of suitable relative permittivity to support electromagnetic propagation in an inherently low-loss waveguide mode. In such a mode, the dielectric core (in this case, the alumina ribbon) acts as a surface waveguide: The interaction of the propagating electromagnetic wave with the dielectric core (and thus the attenuation) is minimal because the field configuration of the mode is such that only a small fraction of the electromagnetic energy propagates along the dielectric core while the remaining major part of the electromagnetic energy propagates, parallel to the ribbon, through the surrounding free space.

The attenuation coefficient (α) of a dominant mode guided by a simple solid dielectric waveguide surrounded by lossless dry air depends on the loss factor and the permittivity of the dielectric material as well as the size and shape of the waveguide and the electromagnetic-field configuration in the particular mode. The equation for the attenuation coefficient is

$$\alpha = (8.686\pi/\lambda_0)\epsilon_1 R \tan(\delta_1)$$

where λ_0 is the free-space wavelength in meters, ϵ_1 is the relative permittivity of the dielectric material, R is a ratio between two integrals that depend on the electromagnetic-field configuration in the particular mode, and δ_1 is the loss tangent of the dielectric material. The product $\epsilon_1 R$ is of particular significance and is denoted



Attenuation Coefficients for several dielectric waveguides were computed theoretically for the frequency range of 28 to 40 GHz. Measured values are indicated by a few data points (*, ▲, ●).

the geometric loss factor.

A systematic study involving computation of α for a variety of dielectric materials and cross-sectional geometries was performed. This study led to the following conclusions (among others):

- A ceramic ribbon waveguide can support two dominant modes with no cut-off frequency — a transverse electric (TE)-like mode with most of its electric field aligned parallel to the major axis

of the cross section of the ribbon, and a transverse magnetic (TM)-like dominant mode with most of its electric field aligned parallel to the minor axis of the cross section.

- Unlike the TE-like mode, the TM-like mode is a low-loss waveguide mode as described above. In the TM-like mode, a suitably dimensioned ribbon waveguide made from alumina or other low-loss, high-permittivity ceramic can

exhibit an attenuation coefficient of less than 0.005 dB/m.

- Whereas the geometrical loss factor of a circular rod is very sensitive to changes in diameter, that of a ribbon is insensitive to small changes in cross-sectional area. This signifies that the TM-like mode on the ribbon is very stable in the sense that it is not easily disturbed by geometrical imperfections.

The figure shows measured and calculated attenuation coefficients for the low-loss dominant mode in several different waveguide structures, including alumina

ribbons with an aspect ratio (width-thickness) of 10 and three different loss-tangent values. These and other data show that high-aspect-ratio alumina ribbons are suitable as low-loss waveguides, opening up possibilities for the development of communication systems operating in the 30-to-300-GHz frequency range.

This work was done by Cavour Yeh, Farzin Manshadi, Philip Stanton, Vahraz Jamnejad, William Imbriale, and Fred Shimabukuro of Caltech for NASA's Jet Propulsion Laboratory. Further information is contained in a TSP [see page 1].

In accordance with Public Law 96-517, the contractor has elected to retain title to this invention. Inquiries concerning rights for its commercial use should be addressed to

Technology Reporting Office
JPL

Mail Stop 249-103
4800 Oak Grove Drive
Pasadena, CA 91109
(818) 354-2240

Refer to NPO-21001, volume and number of this NASA Tech Briefs issue, and the page number.

Micromachined Broad Band Light Sources

Chip-based light source operates at high temperatures to produce high-brightness, white light.

NASA's Jet Propulsion Laboratory, Pasadena, CA, and Glenn Research Center, Cleveland, OH

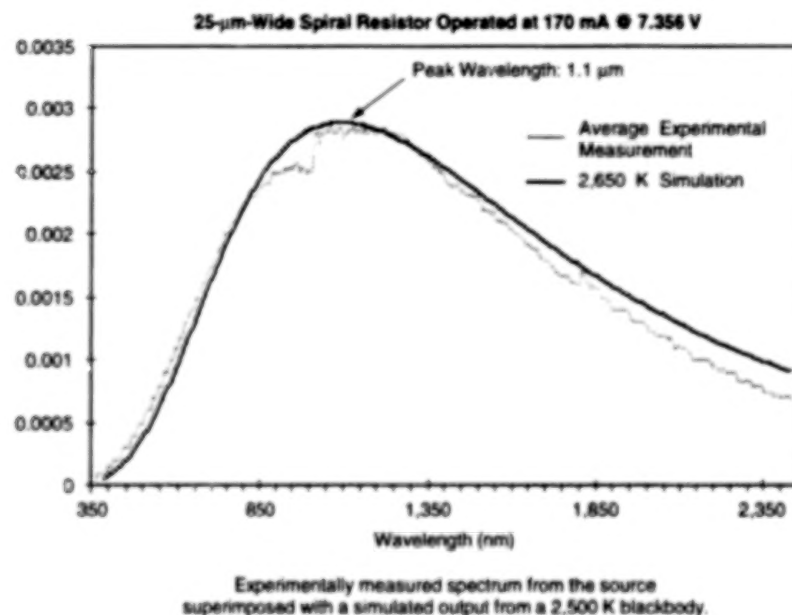


Figure 1. An Experimentally Measured Spectrum is shown from the source superimposed with a simulated output from a 2,500 K blackbody.

A novel micromachined incandescent light source has been designed and fabricated to operate at temperatures exceeding 2,500 K. The high-temperature, tungsten filament-based source has a high-brightness, broad spectral band emission. The monolithic design allows for ease of incorporation with on-chip electronics as well as with fiber optics. Previously micromachined incandescent lamps contained, variously, tungsten or polycrystalline silicon filaments that glowed more dimly because they could only be operated at temperatures between 900 and 1,200 °C. The present devices can be used either in a single (discrete device) or two-dimensional array format for miniature spec-

troscopic instruments and for automotive dashboard displays.

A prototype light source was successfully operated at 2,500 K and has a spectral output closely resembling a simulated blackbody source at the same temperature (see Figure 1). The fabrication process is outlined schematically in Figure 2. The source is based on a modular design and consists of three separately micromachined chips that are subsequently bonded together. The three chips consist of one that includes the tungsten filament, one that includes a reflective mirror, and one that includes an encapsulating, transmission window. Each chip starts out as part

of a Si wafer that is coated with an insulating layer of SiN.

To form the mirror chip, a highly reflective metal is deposited on one face of the wafer. Then a metal ring for subsequent wafer-to-wafer bonding is deposited on the mirror surface. The processing of the filament chip is more complex. First, gold contact pads for the tungsten filament are deposited on one surface of the wafer. An electrically insulating layer of SiO_2 is deposited over the contact pads and the rest of this face. Metal rings for subsequent wafer-to-wafer bonding are deposited on both the SiO_2 layer and the opposite SiN face of the wafer. A central hole destined to become the evacuated light source chamber is patterned and etched through the Si and SiN layers. The SiO_2 layer is patterned and etched to expose the contact pads. The tungsten filament is installed, either by bonding a commercially available thin tungsten wire onto the contact pads, or by attaching a micromachined tungsten filament or by the deposition and patterning of tungsten thin films. Following installation of the filament, the remaining layer of SiO_2 extending within the lamp chamber is etched away. Processing of the window chip begins with the deposition of a bonding ring on face of the wafer. The window is patterned on the bonding-ring face and then the SiN and Si layers are etched away in the window area, leaving only a window of SiN on the face opposite the bonding ring. Finally, the window, filament, and mirror wafers are bonded under vacuum or a controlled atmosphere.

This work was done by Thomas George and Eric Jones of Caltech for NASA's Jet Propulsion Laboratory, in

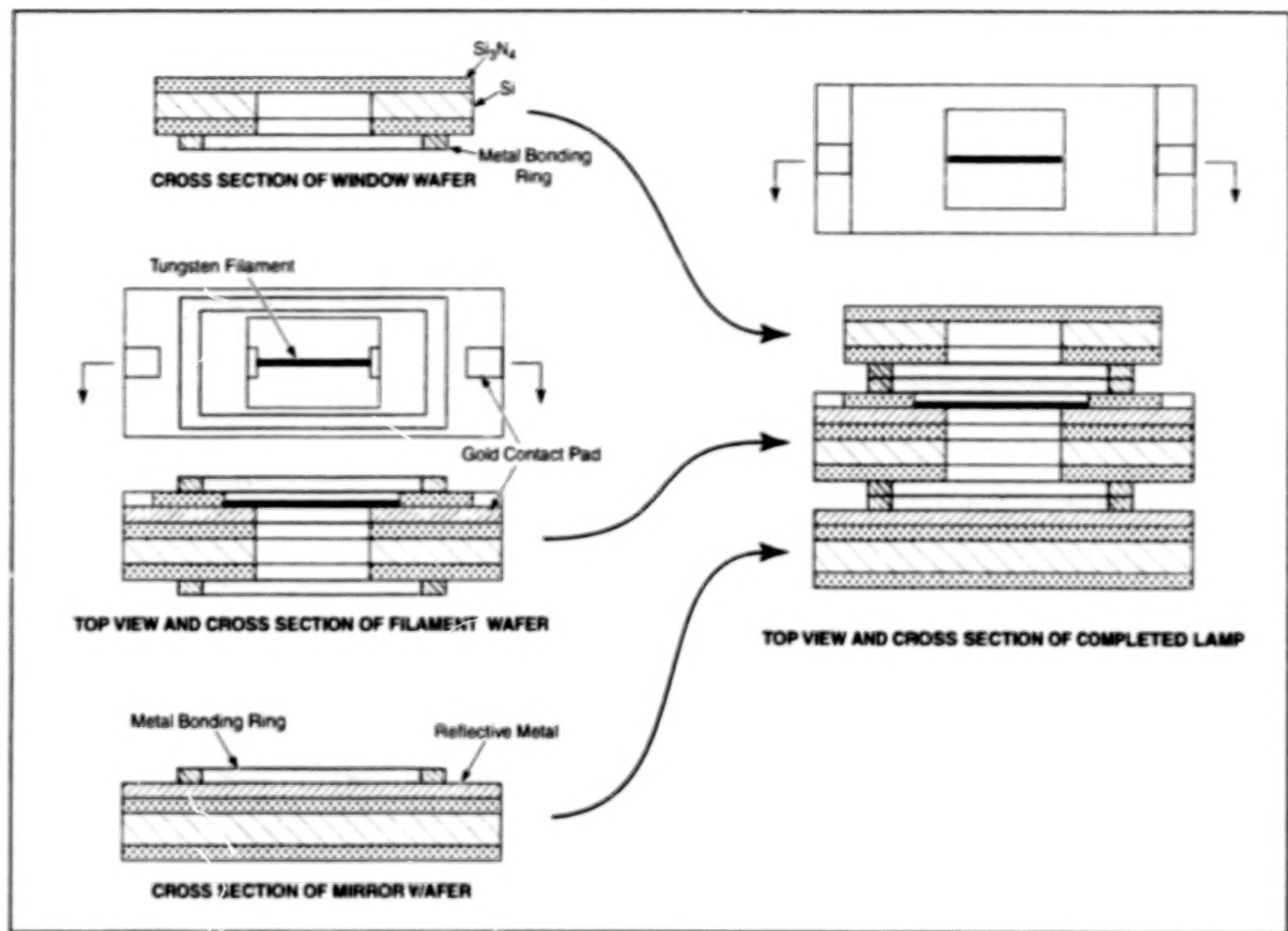


Figure 2. Following a Modular Approach to Design and Fabrication, an incandescent lamp is fabricated by micromachining three wafers, then bonding them together.

collaboration with Margaret Tuma of NASA's Glenn Research Center. Further information is contained in a TSP [see page 1].

In accordance with Public Law 96-517, the contractor has elected to retain title to

this invention. Inquiries concerning rights for its commercial use should be addressed to

Technology Reporting Office
JPL
Mail Stop 122-116

4800 Oak Grove Drive
Pasadena, CA 91109
(818) 354-2240

Refer to NPO-20655, volume and number of this NASA Tech Briefs issue, and the page number.

CMOS Image Sensors Capable of Time-Delayed Integration

This will enable CMOS to perform a function previously limited to CCDs.

Complementary metal oxide/semiconductor (CMOS) image sensors would be capable of operation in a time-delayed-integration (TDI) mode. Heretofore, the only semiconductor electronic image sensors capable of TDI have been charge-coupled devices (CCDs), which have dominated the image-sensor market for nearly all applications.

TDI is an advancement upon so called "push broom" imagers in which a one-dimensional imager array (1×512 , for example) is used from a moving platform such as an airplane or satellite. The long

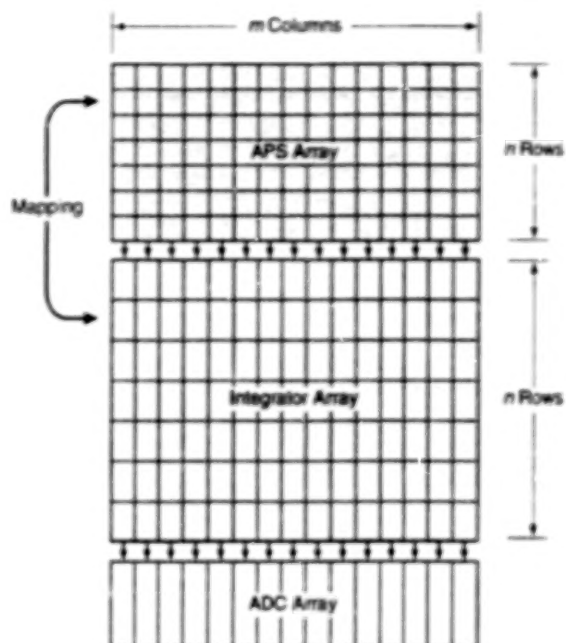
dimension in such imagers is used to divide the ground scene into pixels in the lateral or so-called cross-track direction. Time sampling is used to divide the ground image in the along-track direction.

TDI imagers use a two-dimensional array (32×512 , for example). The imager is still operated from a moving platform using the "push broom" scheme; however, as a ground pixel moves across the pixels of the imager in the along-track direction (along the 32 pixels of the column in the example above), the TDI imager multiply samples the same ground pixel and then

NASA's Jet Propulsion Laboratory,
Pasadena, California

sums or averages these multiple samples in order to improve the signal-to-noise ratio as compared with a simple, one-dimensional push broom imager.

CCDs are ideally suited for TDI, because they use noiseless summing of charge packets, and because the charge packets are naturally moved across the image plane during readout in a CCD. It is a simple matter to essentially move the charge packet in time with the motion of the associated ground pixel. Unfortunately, CCDs are inherently fairly high-power devices (consuming on the order of watts) and



TDI Would Be Implemented in CMOS Circuitry on the basis of an architecture in which APS pixel rows would be mapped to the rows in the array of integrators.

their fabrication processing is not fully compatible with integrated CMOS electronics. CMOS imagers have the ability to operate with much lower power (on the order of tens of milliwatts) and allow the integration of control electronics and signal processing on-chip, in order to enable the development of highly compact complete imaging systems, including even analog-to-digital conversion on-chip.

The development of low-noise switched capacitor circuitry, as well as the development of the CMOS active pixel sensor (APS) visible imager, have made it possible in principle to realize TDI in the proposed CMOS image sensors. As shown in the figure, a device according to the proposal would include a CMOS 32×512 APS array connected column-wise to a $32 \times$

512 array of low-noise, high-speed analog charge integrators. These are followed by a one-dimensional array of column-parallel cyclic architecture analog-to-digital converters that service the column-parallel array of integrators.

As a ground pixel moves its focus from pixel to pixel along the column of the APS array, the signal from this ground pixel is multiply sampled, and each sample is integrated onto the storage capacitor on one integrator in the integrator array. Since the ground pixel moves from pixel to pixel in the imaging array, the TDI imager must continually keep track of which pixel's output is added to which integrator. After a given ground pixel has moved through all 32 rows, the output of the corresponding integrator is sent to the ADC for digitization.

tion, and the integrator is reset so that it can begin the integration of the new ground pixel that moves into the field of view. Of course, all 32 pixels in the column must be connected in turn to the appropriate integrators in the time it takes for a ground pixel to move from one imager pixel to the next. The signal is dumped in a snapshot mode that eliminates motion artifacts that would otherwise be caused by the fact that each imager pixel is addressed at a slightly different time.

Within the general layout and mode of operation described above, the proposal encompasses several alternative operating schemes and readout-circuit designs. Each represents a different trial solution to achieve optimum performance with regard to sensitivity, low power consumption, high-speed digital readout, and minimization of the non-imaging-area of the chip. These schemes and designs are too complex to describe within the space available for this article; interested readers should request more information, as noted below.

This work was done by Bedabrata Pain, Thomas Cunningham, Guang Yang, Monica Ortiz, and Brita Olson of Caltech for **NASA's Jet Propulsion Laboratory**. Further information is contained in a TSP [see page 1].

In accordance with Public Law 96-517, the contractor has elected to retain title to this invention. Inquiries concerning rights for its commercial use should be addressed to

Technology Reporting Office
JPL
Mail Stop 249-103
4800 Oak Grove Drive
Pasadena, CA 91109
(818) 354-2240

Refer to NPO-20802, volume and number of this NASA Tech Briefs issue, and the page number.

Leakage-Preventing Design of Snapshot Photodiode CMOS Imager

Other improvements would include increased fill factor and reduced readout noise.

A new design for a complementary metal oxide/semiconductor (CMOS) snapshot imaging device of the photodiode-based, active-pixel-sensor (APS) type calls for features to prevent photogenerated electric charges collected during a given frame period from leaking into in-pixel capacitors that store charges collected during the preceding frame period, pending completion of readout from that period.

The proposed design would also utilize the electronic-shuttering capability of an APS to provide for programmable exposure time, down to ($\sim 10 \mu\text{s}$) a small fraction of the frame period, to enable faithful recording of images of rapidly moving objects. Finally, the design would make it possible to obtain quantum efficiency higher and readout noise lower than those of a typical prior CMOS APS imaging device.

NASA's Jet Propulsion Laboratory, Pasadena, California

The circuit in each pixel of a typical CMOS snapshot imaging device (see Figure 1) includes a storage capacitor (C_p) that serves as both a frame buffer memory (as described above) and a sensing node. The photodiode in this circuit converts incident photons to electrons during an exposure time that is defined as the time during which transistor switch RST-D is kept open. The possibility of controlling

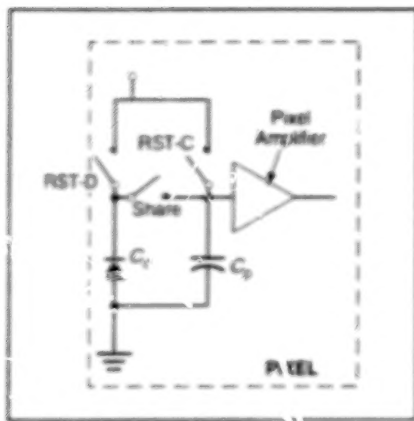


Figure 1. The Pixel Circuitry in a CMOS APS imaging device includes (a) a capacitor that acts as a frame buffer memory and (b) provisions for electronic shuttering.

this time by controlling the duration of a pulse that controls RST-D (in other words, electronic shuttering) is what makes it possible to set the exposure time at any desired fraction of the frame period.

During the exposure, photoelectrons are stored temporarily in the photodiode capacitance (C_D). After the exposure, C_D is reset (that is, purged of the charge from the preceding frame period) by momentary closing of transistor switch RST-C. During this reset, part of the charge accumulated in C_D during the just-completed exposure is transferred to C_P by momentary closing of the transistor switch labeled "Share." Once this transfer of charge has been completed, the photodiode is available to begin a new frame exposure, and the charge newly transferred to C_P is held there until it is read out at its assigned time in a row-by-row readout sequence that is completed before the beginning of the next frame period.

The design and operation of a typical prior CMOS snapshot imager as described thus far raise three main concerns that are addressed by the proposed design:

1. The leakage mentioned above is an unwanted lateral diffusion of charge from C_D to C_P during exposure. This leakage is deleterious because it gives rise to image smear and, in the case of movement in the image, it introduces motion-related artifacts.

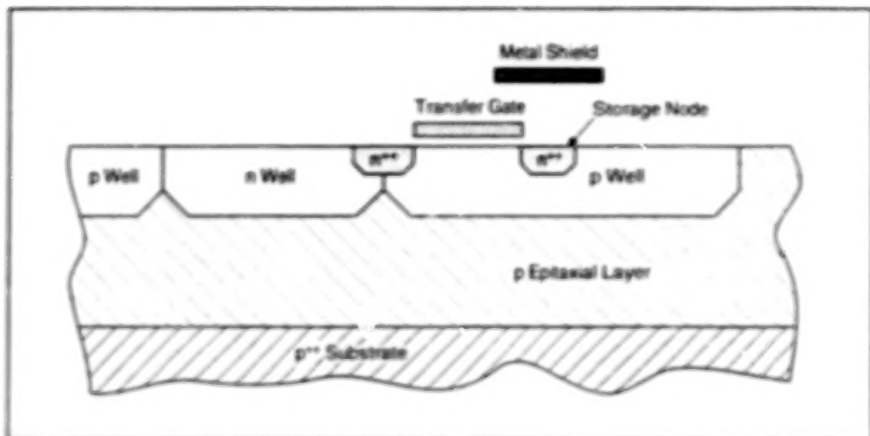


Figure 2. This Cross Section of a Pixel according to the proposed design depicts features that would give rise to an electric field that would prevent leakage.

2. The transistor switches and the storage capacitor in each pixel reduce the fill factor (the fraction of pixel area devoted to photodetection), thereby reducing quantum efficiency.
3. Readout noise includes significant contributions from resetting of C_D , resetting of C_P , and sharing of charge between C_D and C_P .

In the proposed design (see Figure 2), the pixel circuit elements would be configured to create an electric field that would prevent the diffusion of photoelectrons into C_P . The design would be implemented in a twin-well process with a lightly doped epitaxial layer to ensure excellent collection of photoelectrons. The n well would act as a photodiode, and the storage capacitance would be implemented in the p well as a diffusion or a gate capacitance. The transfer gate would be driven by the "Share" transistor switch as in Figure 1. The storage node would be shielded by metal to maintain the integrity of stored photocharges. The storage node in the p well would be held at ground potential. Hence, electrons generated in the p epitaxial layer or the n well (which would be biased above ground) would be prevented, by the resulting potential barrier, from reaching the storage node. Furthermore, the n++-doped subregion in the storage-node region would be reverse-biased, so that no holes would reach it. Holes would be drained at a p++

contact (not shown in the figure) in the p well. Thus, the storage node would be protected against any coupling from the photodiode, enabling smearless imaging.

A major characteristic of this configuration is that the storage capacitance per unit area would be orders of magnitude greater than that in a corresponding prior design, so that it would be possible to make C_P occupy a much smaller area; hence, there would be plenty of margin to choose whatever value of C_P is needed to minimize readout noise, without risk of significantly degrading the fill factor and thus the quantum efficiency along with it. (The optimum choice of C_P to minimize readout noise turns out to be between 0.7x and 1x C_D .)

This work was done by Bedabrata Pan of Caltech for NASA's Jet Propulsion Laboratory. Further information is contained in a TSP [see page 1].

In accordance with Public Law 96-517, the contractor has elected to retain title to this invention. Inquiries concerning rights for its commercial use should be addressed to

Technology Reporting Office

JPL

Mail Stop 249-103

4800 Oak Grove Drive

Pasadena, CA 91109

(818) 354-2240

Refer to NPO-21044, volume and number of this NASA Tech Briefs issue, and the page number.

12

BLANK PAGE



Electronic Systems

Hardware, Techniques, and Processes

15 Automatic Bias Compensation in GPS Receivers

14

BLANK PAGE

Automatic Bias Compensation in GPS Receivers

Errors caused by unintended variations in electronic components are corrected.

A technique of automatic bias compensation has been devised to correct errors caused by variations among electronic components in Global Positioning System (GPS) receivers that use the coarse/acquisition (C/A) GPS code. Even though there are large government and commercial markets for such GPS receivers, these errors have not been generally understood. [Alternatively or in addition to the automatic-bias-compensation technique, the errors can be reduced by (1) building GPS receivers from components of higher quality (that is, components that have lower manufacturing tolerances and are less sus-

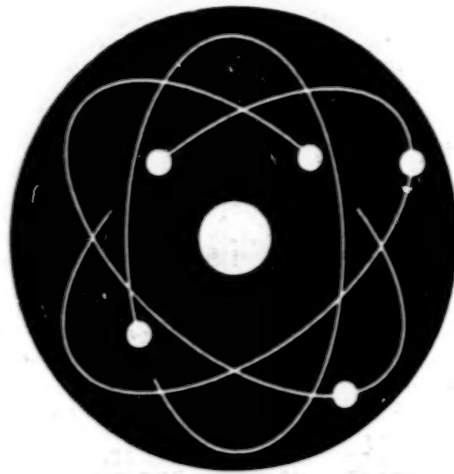
ceptible to aging) and (2) performing more extensive manual adjustments during integration and testing of GPS receivers.]

The errors in question are sampler biases, which can interact with GPS signals in such a way as to introduce spurious signals that can confuse affected receivers. The effect of these errors is more pronounced at the high Doppler shifts in signals received by a GPS receiver aboard an orbiting spacecraft or other high-speed vehicle. The automatic-bias-compensation technique is implemented in the digital signal-processing portion of a GPS receiver. The digital samples of amplified received

NASA's Jet Propulsion Laboratory,
Pasadena, California

signal + noise are measured for a bias. Corrections are computed and written over the incoming samples to drive the resulting bias to zero, which also reduces the signal-to-noise level. This process is controlled by a feedback loop to adapt automatically to variations in the level of uncorrected bias coming from the sampler.

This work was done by Lawrence Young, Jeffrey Tien, and George Purcell of Caltech for NASA's Jet Propulsion Laboratory. Further information is contained in a TSP [see page 1]. NPO-20819



Physical Sciences

Hardware, Techniques, and Processes

- 19 Biomimetic Gliders
- 20 High-Heat-Flux Thermogravimetric Analysis With Radiography
- 21 Thermogravimetric Analysis With Laser Heating
- 22 High-Speed Image Compression via Optical Transformation
- 22 High-Speed Optical Image Compression at Lower Power
- 23 Confocal Single-Mode-Fiber-Optic Raman Microspectrometer
- 24 Microsphere and Microcavity Optical-Absorption Sensors
- 26 Coarse Alignment of a Segmented Telescope Mirror
- 27 Highly Oblate Microspheroid as an Optical Resonator

Books and Reports

- 27 Ultralight Balloon Systems for Exploring Uranus and Neptune

Biomimetic Gliders

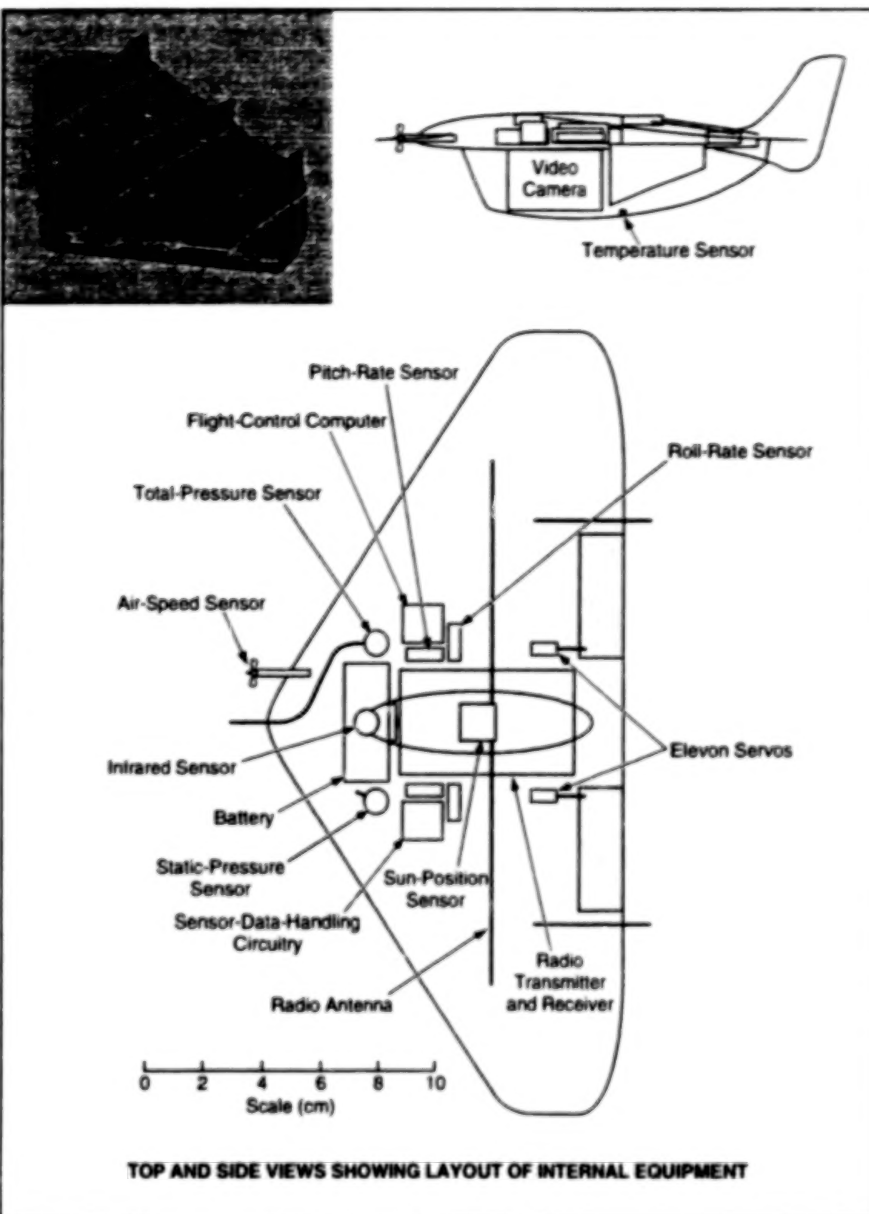
Miniature robotic microflyers would gather scientific data to enable reconnaissance missions and deploy payloads on landing.

NASA's Jet Propulsion Laboratory,
Pasadena, California

Biomimetic gliders are small robotic microflyers proposed for use in scientific exploration of planetary atmospheres and terrains that capture some key features of insect and bird flight. Biomimetic gliders as biomimetic flight systems are a subset of biomimetic explorers. The multidisciplinary system concept of "Biomimetic Explorers" represents small, dedicated, low-cost explorers that possess some of the key features of biological systems, not easily captured by conventional robotic systems. Such features particularly include versatile mobility, adaptive controls, bioinspired sensor mechanisms, biomimetic sensor fusion, biomimetic communications, biomimetic cooperative behavior, distributed operations, and biomimetic energy generation/conversion. Significant scientific and technological payoff at a low cost is realizable by using the potential offered by a large number of such cooperatively operating biomimetic explorer units in concert with the traditional exploration platforms such as the lander/rover, orbiter, etc., for example.

Biomimetic Explorers and some concepts on biomimetic surface/subsurface systems have been described in several previous articles in *NASA Tech Briefs*, the most relevant being "Biomimetic Explorers" (NPO-20142), Vol. 22, No. 9, (September 1998), page 71; "Earthwormlike Exploratory Robots" (NPO-20266), Vol. 22, No. 6, (June 1998), page 11b; and "Insectile and Vermiform Exploratory Robots" (NPO-20381), Vol. 23, No. 11, (November, 1999), page 61. Particularly, the biomimetic glider is a small, simple, low-cost system ideal for distributed measurements, reconnaissance, and wide-area dispersion of sensors and small experiments.

The key specifications/features of a biomimetic glider include: mass of 100 to 500 g, payload fraction > 50 percent, large range of aerial mobility of 10 to 100 km, volume 300 to 5,000 cm³, active flight control, solar navigation, soaring flight using atmospheric energy, cooperative mission using from 10 to 30 gliders providing coverage of area of about 100 × 100 km. The glider is particularly suitable for deployment in large numbers to perform reconnaissance over large areas. A typical biomimetic glider (see figure) would be equipped with sensors (meteorological instrumentation such as temperature, pressure, solar irradiance, and moisture sensor, etc.,



TOP AND SIDE VIEWS SHOWING LAYOUT OF INTERNAL EQUIPMENT

A Biomimetic Glider would carry miniaturized equipment for flight control, navigation, communication, and scientific observation/analysis.

and/or miniature imagers for close-up imaging of the terrain) sensory-data-handling circuitry, flight-control actuators, control circuitry, and a radio transmitter and receiver. A biomimetic glider could navigate autonomously (e.g., by reference to the direction of the Sun). In a typical operation, multiple biomimetic gliders would be released from an aircraft or spacecraft in orbit/fly-by mode at an altitude of several kilometers and sent off to explore in different directions. Alternatively, they could be launched from a Lander to inspect a number of sites and provide valuable informa-

tion to allow selection of the best site for further probing by the rover. Biomimetic gliders could thereby enable enhanced data return for sample-return reconnaissance missions and provide a new capability for distributed measurements.

Additionally, the time aloft could be prolonged by controlling a biomimetic glider to utilize atmospheric energy in the same manner as that of soaring birds and particularly soaring insects that migrate large distances using such a capability.

During the flight of a biomimetic glider, the onboard instrumentation could gather

er data on the atmosphere and terrain. Images acquired by a small onboard video camera could contribute data for maps of the terrain, could be processed to identify targets for closer examination, and/or used to guide the glider to a landing at a chosen target site. A variety of

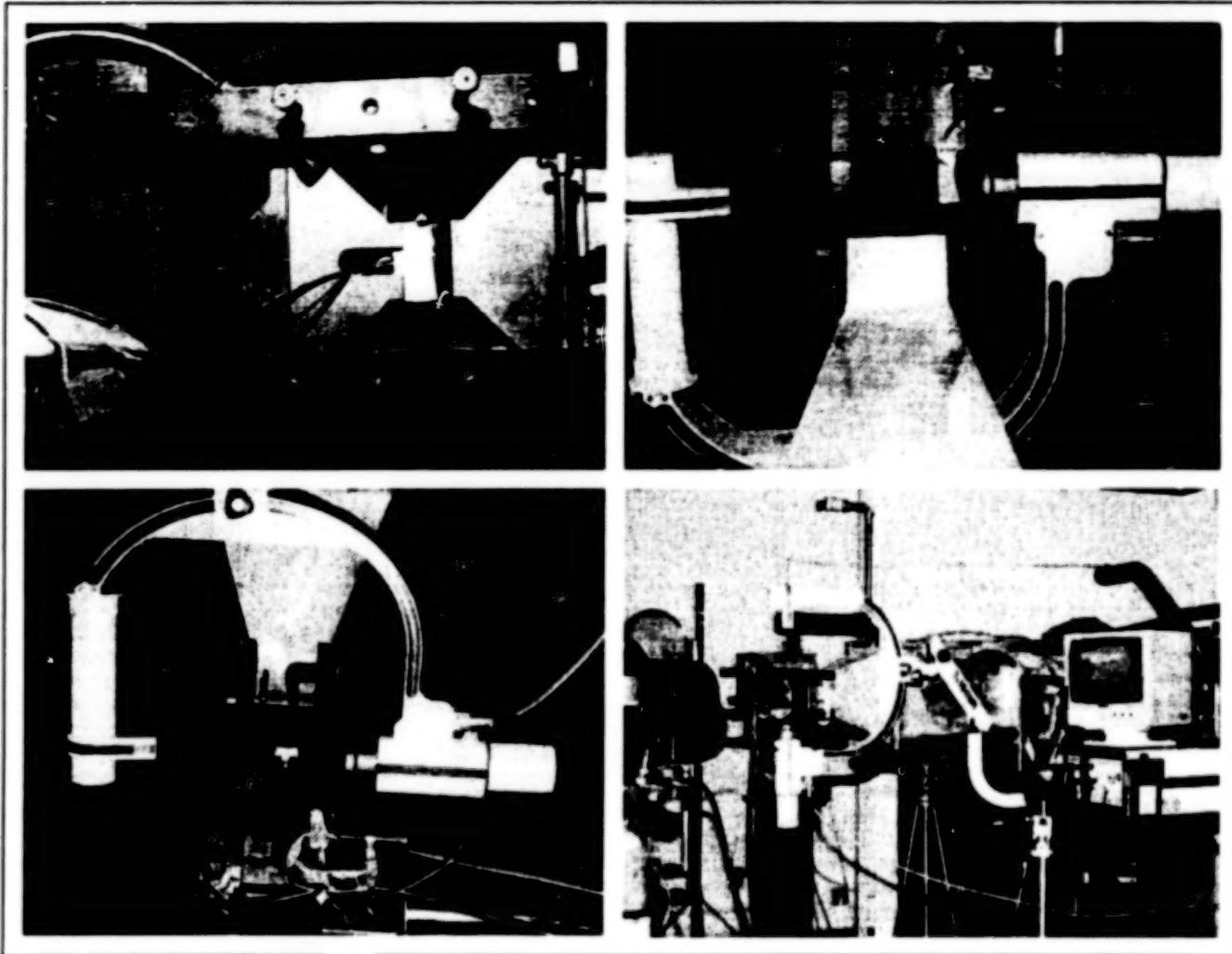
surface instruments/experiments could be deployed by the glider on landing. The results of the analysis would be transmitted to a relay point, which could be, for example, a receiver aboard the lander or the aircraft/spaceship from which the glider was released.

This work was done by Sunita Thakoor of Caltech and Carlos Miralles of AeroMtron for NASA's Jet Propulsion Laboratory. Further information is contained in a TSP [see page 1].
NPO-20677

High-Heat-Flux Thermogravimetric Analysis With Radiography

Test conditions are relatively realistic.

Marshall Space Flight Center,
Alabama



This **Laboratory Setup** has been used to perform RTR-TGA experiments on specimens of a laminated composite material representative of materials in the nozzles of solid-fuel rocket motors.

A process and a laboratory setup to implement the process (see figure) have been devised to enable the acquisition of time-resolved data on the thermal decomposition of a specimen of a solid material exposed to a heat flux comparable to the heat flux in a typical rocket engine. The process is called "RTR-TGA" because it includes a combination of real-time radiography (RTR) and thermogravimetric analysis (TGA). In the process, one specimen surface (e.g., representing a surface exposed

to flames in a rocket engine) is heated by a continuous-wave CO₂-laser beam while the interior temperature of the specimen is measured and the specimen is observed by an x-ray apparatus that produces video images that can be recorded. The major advantage of this process over older processes for observing thermal decomposition of material specimens is that the environment to which the specimen is exposed approximates more closely the heating environment in a full-scale rocket engine.

The specimen must be instrumented with a thermocouple for measurement of its interior temperature. Experiments at different heating rates can be performed by changing the power output of the laser and/or by changing the depth at which the temperature is recorded. The closer a thermocouple is to the irradiated surface of the specimen, the higher is the heating rate observed. Specimens tested to date have been made of a composite material with 90° ply angles and overall dimen-

sions of 1.5 in. (38 mm) in height and width and 0.75 in. (19 mm) in thickness. Thermocouples have been installed in these specimens, oriented parallel to the irradiated surfaces in the cross-ply directions, at depths of 1/8 in. (3 mm), 1/4 in. (6 mm), and 3/8 in. (9.5 mm) from the irradiated surfaces.

The special fixture for holding the specimen is designed to exclude any extraneous material from the radiographic field of view of the specimen. The fixture is also designed to minimize any "funneling" of the photons and to restrain the specimen against any motion that might be induced by thermal expansion. The fixture is further designed to allow access for electrical connection to the thermocouple in the specimen.

In preparation for an experiment, a specimen containing a buried thermocouple is placed in the fixture. A C-shaped arm that is part of the radiographic apparatus is then positioned for scanning; guidance for positioning is obtained by turning on the radiographic apparatus and observing real-time x-ray images as the arm is maneuvered.

In the experiment, the specimen surface of interest is completely exposed to the laser beam. Exposures to date have been 20 seconds in duration with incident laser-beam power densities of 300 and 400 W/cm² laser incidence. The radiographic

and thermocouple data are recorded from about 5 seconds before to about 1 minute after turn-on of the laser beam.

The recorded radiographic images are digitized, then digitally processed to obtain a density profile of the specimen as a function of time. The density data at the depth of the thermocouples are then plotted against the temperatures measured by the thermocouples to obtain an industry-standard density-vs.-temperature plot.

This work was done by Tim Johnson of Thiokol Corp. for Marshall Space Flight Center.

MFS-31365

Thermogravimetric Analysis With Laser Heating

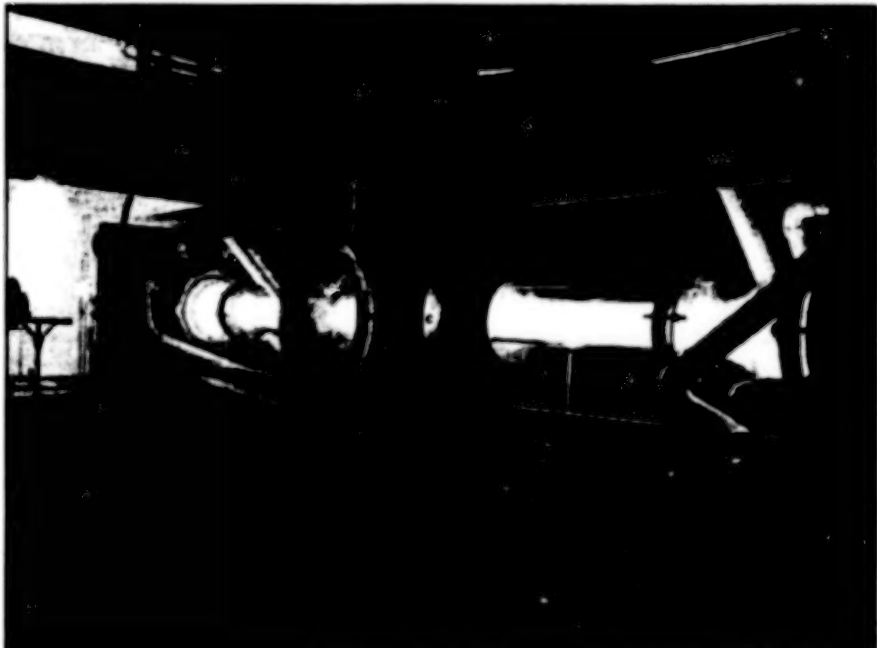
A thin specimen is radiantly heated from both sides.

Laser thermogravimetric analysis (laser TGA) is a technique that yields time-resolved data on the thermal decomposition of a specimen of a solid material exposed to a heat flux comparable to the heat flux in a typical rocket engine. Like the technique described in the preceding article, laser TGA involves heating the specimen with a continuous-wave laser beam to obtain the required high heat flux. The utility of laser TGA is not restricted to rocket-engine materials; laser TGA could be used to study high-heating-rate thermal decomposition of almost any high-temperature insulating material.

The laser beam must have a flat distribution of power over its cross section. The beam power delivered to the specimen may lie between 1 and 10 kW. The specimen is mounted on a custom-designed scale that (1) measures the loss of weight of the specimen as the specimen thermally decomposes and (2) is also instrumented to measure the time-varying temperature of the specimen. The scale and specimen are placed in a stainless-steel chamber that is purged with argon to provide a chemically inert environment. The laser beam is split into two equal-power beams by use of a half-reflective mirror. The two beams enter the chamber through salt windows on opposite sides (see figure), and impinge on opposite faces of the specimen.

The specimen is fabricated as a circular wafer. The thickness of the wafer is

Marshall Space Flight Center,
Alabama



CO₂-Laser Beams in Tubes enter the test chamber through salt windows on opposite sides. A third salt window can be used for observation by an infrared camera, or optical pyrometer.

chosen according to the thermodynamic properties of the specimen material. The specimen should be made as thin as practicable. The exposure of both sides of the very thin specimen to equal irradiance provides essentially uniform heating with no appreciable thermal gradients across the thickness.

During an experiment, the temperature and the weight-loss data are recorded and

plotted against each other to obtain an industry-standard density-vs.-temperature plot. The experiment can be conducted at various heating rates by changing the power output of the laser.

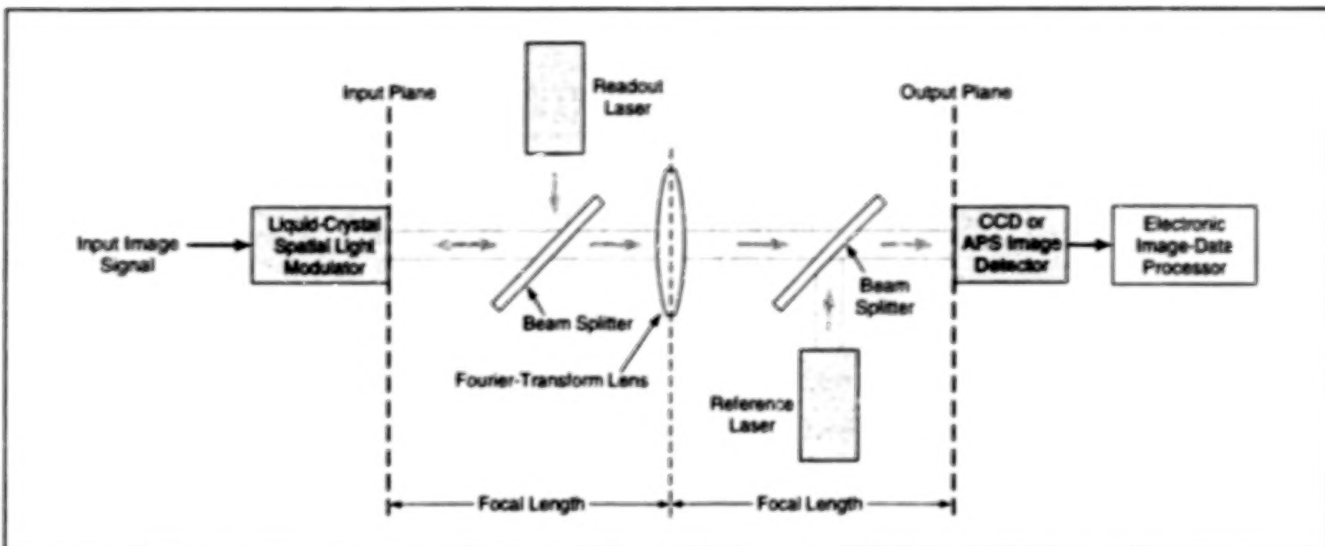
This work was done by Tim Johnson of Thiokol Corp. for Marshall Space Flight Center.

MFS-31366

High-Speed Image Compression via Optical Transformation

A lens would be utilized as an optical Fourier transformer.

NASA's Jet Propulsion Laboratory,
Pasadena, California



The Lens, Lasers, and Beam Splitters would be positioned to generate a hologram containing a Fourier transform of the input image. The optical propagation time to form the hologram would be much shorter than the time needed for digital electronic computation of the Fourier transform.

A proposed method of compressing image data would exploit the well-known capability of a converging lens to generate the Fourier transform of an image by purely optical means, in much less time than is needed to compute the discrete Fourier transform of a sampled image by use of digital electronic circuits. Inasmuch as a transform (whether of the Fourier, discrete-cosine, or other type) is the most computation-intensive part of almost any electronic image-compression scheme, the speedup afforded by the proposed method could make the difference between success or failure in applications in which there are requirements to compress image data at high throughput rates. In addition, because high-speed digital image-processing circuits are typically power-hungry, the use of optical Fourier transformation can reduce power consumption.

The Fourier-transform property of a converging lens can be summarized as follows: When the lens is placed at its

focal distance from both an input and an output plane, then the image formed by the lens on the output plane is a Fourier transform of the object or image at the input plane. The two-dimensional spatial-frequency vector associated with any given point in the output image is proportional to the position vector from the optical axis to that point.

In the proposed method (see figure) the input image would be generated on a liquid-crystal spatial light modulator illuminated with a readout laser, which would be coherent with a reference laser. (It would be necessary to generate the input image in this way because the coherence of the laser light would be needed to form a hologram described subsequently.) A lens would be located at its focal distance from the input plane as well as from the output plane, where a charge-coupled-device (CCD) or an active-pixel sensor (APS) would be placed to detect the image. As a result,

the Fourier transform of the input image would be formed on the image detector.

Capturing the intensity magnitude at the detector is not sufficient for reconstructing the image. For this reason, it would be necessary to write a hologram onto the image detector by means of interference between the lens-transformed image beam and the reference laser beam.

Because most of the information in a typical image is concentrated at low spatial frequencies, the bulk of information in optical Fourier transform would be concentrated about the optical axis. The image detector would sample the Fourier transform. The samples would be digitized, then entropy-coded by use of established digital electronic techniques.

This work was done by Deborah Jackson of Caltech for NASA's Jet Propulsion Laboratory. Further information is contained in a TSP [see page 1].
NPO-20638

High-Speed Optical Image Compression at Lower Power

White-light holography would enable elimination of a power-hungry spatial light modulator.

In an alternative to the optical image-compression method of the preceding article, the Fourier transform of the input image would be formed on the output plane by white-light holography, instead of

by laser holography. The principal advantage of the alternative method would be decreased power consumption: A state-of-the-art liquid-crystal spatial light modulator needed to implement the method of the

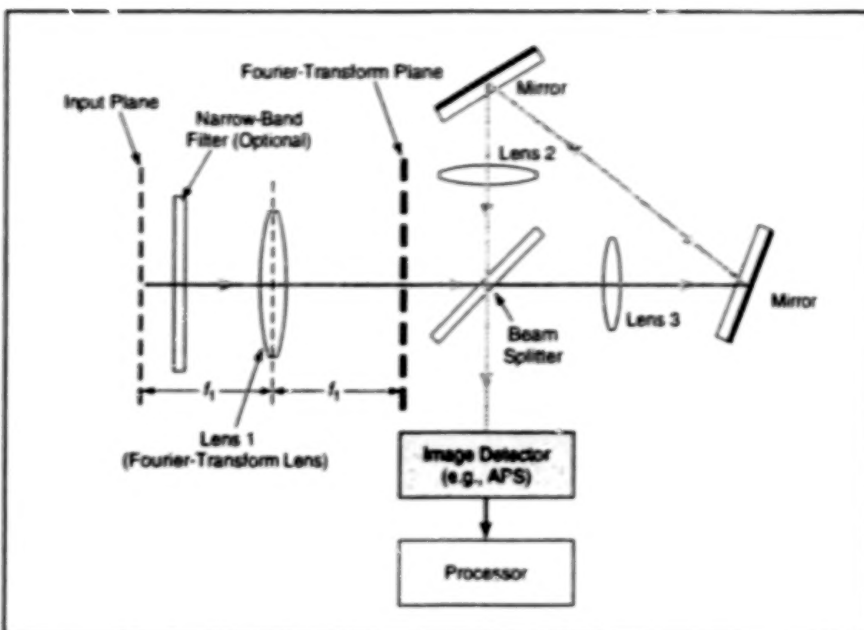
NASA's Jet Propulsion Laboratory,
Pasadena, California

preceding article consumes about 10 W of operating power, and the liquid crystals must be maintained at a temperature near 25 °C. On the other hand, an image detector of the active-pixel-sensor (APS) type,

needed to acquire the Fourier-transform image in both the method of the preceding article and in the alternative method, consumes only about 50 mW. Because the spatial light modulator would not be needed in the alternative method, the power consumption of the image-compression system could be greatly reduced.

In the alternative method (see figure), the input image could be formed in sunlight or any other suitable incoherent light. A lens would act as an optical Fourier transformer, but in this case, two slightly different white-light Fourier-transform images would be made to interfere with each other to form a white-light hologram. An interferometric loop would extract the relevant phase information. The particular configuration of the interferometric loop, originally developed for white-light holography, would simultaneously optimize the spatial and temporal overlap of the input intensity pattern, as needed to obtain a measurable contrast for white-light interference. Different magnifications would be used along the clockwise and counterclockwise circuits of the interferometer, in order to make each point in the image interfere with itself; this design would eliminate the need for a spatial light modulator and lasers to obtain the coherence needed to generate a hologram. The design problem then becomes one of matching the contrast ratio of the white-light hologram with the dynamic range and offset of the image detector.

The input image would be presented at the left focal plane of the Fourier-transform lens, which would have a focal length f_1 . The Fourier-transform image would be formed at a distance f_1 to the right of this lens, at the entrance to the interferometric loop. Within the interferometric loop, two lenses with differing focal lengths of f_2 and f_3 , respectively, would refocus the Fourier-transform image onto the image detector at two different magnifications. The magni-



Two White-Light Fourier-Transform Images with different magnifications would be made to interfere with each other to obtain a white light hologram on the detector plane.

fication of the clockwise circuit would be f_3/f_2 , while that of the counterclockwise circuit would be f_2/f_3 . Components of the light that came from the same point in the Fourier-transform plane would interfere on the detector plane and thereby provide phase information. Light coming from different points in the Fourier-transform plane would be superimposed incoherently on the detector plane. As in the method of the preceding article, the low-spatial-frequency image information would be concentrated about the optical axis on the detector plane.

The major drawback of white-light holography is that the coherently interfering waves comprise only a small fraction of the total light, so that interferograms are unavoidably superimposed on bright backgrounds. The use of an electronic (as opposed to a photographic-film) image

detector would make it possible to process the image information electronically to remove the bright background. Implementation would involve a formidable challenge in that it has been estimated that 50 dB of dynamic range would be needed to eliminate the background signal while an additional 30 dB of dynamic range would be needed to achieve 10-bit precision in pixel readouts. One could use a narrow-band filter to reduce the brightness of the background light and increase the coherence length of the light to obtain more margin for design specifications.

This work was done by Deborah Jackson of Caltech for NASA's Jet Propulsion Laboratory. Further information is contained in a TSP [see page 1].
NPO-20639

Confocal Single-Mode-Fiber-Optic Raman Microspectrometer

Improvements would include compactness, increased spatial resolution, and superior rejection of laser light.

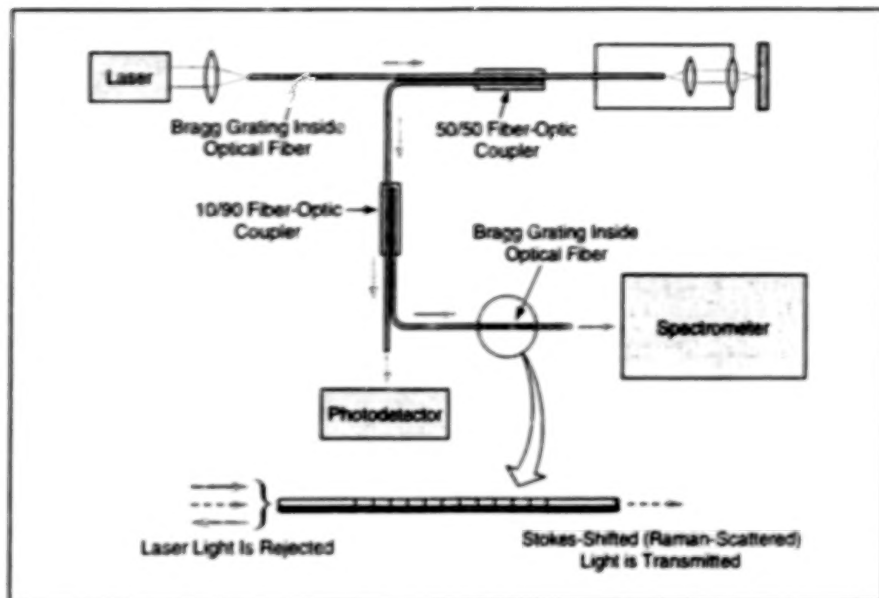
A proposed optoelectronic apparatus would perform the combined functions of a confocal microscope and a Raman spectrometer. It would be used to acquire Raman-spectral-image and/or monochromatic-image data from mineral and/or biological specimens with high three-dimensional spatial resolution. The Raman-spectral-image data could be used to identify materials present at var-

ious locations within the specimens.

By virtue of the confocal-microscope aspect of its design and unlike prior Raman probes, the proposed apparatus would offer sufficient spatial resolution for imaging of microscopic objects and sufficient depth discrimination to enable sectioning; that is, the apparatus could be used to construct the equivalent of three-dimensional images from confocal-microscope scans in three

NASA's Jet Propulsion Laboratory, Pasadena, California

dimensions. The spectrometer portion of the apparatus would be compact, relative to prior Raman spectrometers of equivalent spectral resolution. The design of the apparatus would also implement a unique solution to the problem of discriminating between Raman-scattered light and laser light used to excite Raman scattering — a difficult problem in that the Raman spectral shift can be small.



The Confocal Single-Mode-Fiber-Optic Raman Microspectrometer would incorporate several improvements over prior Raman probes, including scanning Raman spectrometers that contain multimode optical fibers.

The figure depicts one version of the proposed apparatus. Light from a laser or a laser diode would be launched into a single-mode optical fiber configured as an input port (port 1) of a nominal 50/50 fiber-optic directional coupler. One of the output ports (port 3) of the coupler would not be used. Another single-mode optical fiber configured as an output port (port 2) would couple the laser light into a compact scanning head that would contain an objective lens assembly. The light diverging from the output end of this fiber would be focused by the objective lens onto a small spot on the surface of a specimen (or, optionally in the case of a semitransparent specimen, into a small subsurface volume). Light reflected from the specimen (including Raman-scattered light) would be focused by the objective lens assembly into the fiber, where it would travel back toward the 50/50 coupler. The portion of the reflected light coming out of port 4 of the 50/50 coupler would be split by a 10/90 fiber-optic splitter; the weaker output would be sent to a photodetector and the stronger to a Raman spectrometer.

This apparatus would differ substantially from prior Raman probes in which scanning heads are coupled by use of multimode optical fibers.

mode optical fibers. Because of its single-mode nature and small diameter (a few micrometers), the core of the optical fiber ending in the scanning head could be considered a pinhole, which, in combination with the objective lens, would afford the resolution needed for confocal microscopy with the depth discrimination needed for three-dimensional imaging and spectroscopy of semitransparent objects. In contrast, coupling by use of multimode optical fibers results in much coarser resolution — both laterally and in depth.

Another important difference between this apparatus and prior Raman probes would lie in the manner of discriminating between Raman-scattered and laser light. In other Raman probes, laser light is often rejected from spectrometer-input paths by use of combinations of notch and edge filters. In the proposed system, a Bragg grating incorporated into the core of the optical fiber going to the spectrometer would serve as a high-resonance-quality (high-Q), in-line rejection filter that would block light in a narrow band centered at the laser wavelength while passing the remainder of the spectrum. (A Bragg grating could function in this way only within a single-mode optical fiber; it could not do so in a multimode

fiber.) The degree of rejection of laser light could be more than 80 dB.

It would be necessary to compensate for the temperature sensitivities of the narrow-band rejection filter and the laser because if the laser wavelength were to drift from the rejection wavelength, then too much laser light would get through to the spectrometer. The use of fiber Bragg gratings would offer a convenient solution to this temperature-compensation problem: Another Bragg grating, of relatively low reflectivity, located in the optical fiber between the laser and port 1 of the 50/50 directional coupler, would be used to lock the laser wavelength; the laser wavelength would be controlled by the reflection band of this grating, which could be made to match the rejection band of the Bragg grating in the fiber going to the spectrometer. The portions of the optical fibers containing these gratings could be mounted in contact with a common heat sink and thereby maintained at the same temperature.

Yet another notable aspect of the proposed apparatus would be the aforementioned relative compactness of the spectrometer. This compactness would be achieved by a novel design featuring only two reflective surfaces, one of which would be a convex diffraction grating shaped and blazed by electron-beam lithography in poly(methyl methacrylate).

In the version of the apparatus depicted in the figure, the fiber end could be translated along the fast direction of the scan relative to the specimen by use of a microelectromechanical (MEM) scanning mechanism. In an alternative version, the fiber end would be held stationary and a MEM scanning mechanism within the head would translate a small scanning corner reflector that would function in conjunction with a stationary folding mirror and an objective lens assembly. The other directions of the scan can be provided by ordinary piezoelectrics or other means.

This work was done by Pantazis Mouroulis, Mehdi Vaez-Iravani, and Frank Hartley of Caltech for NASA's Jet Propulsion Laboratory. Further information is contained in a TSP [see page 1].

NPO-20932

Microsphere and Microcavity Optical-Absorption Sensors

Chemicals of interest could be detected at low concentrations in small samples.

Miniature high-resolution optical-absorption sensors for detecting trace amounts of chemical species of interest in gas and li-

quid samples are undergoing development. The transducer in a sensor of this type is a fiber-optic-coupled optical resonator in the

NASA's Jet Propulsion Laboratory, Pasadena, California

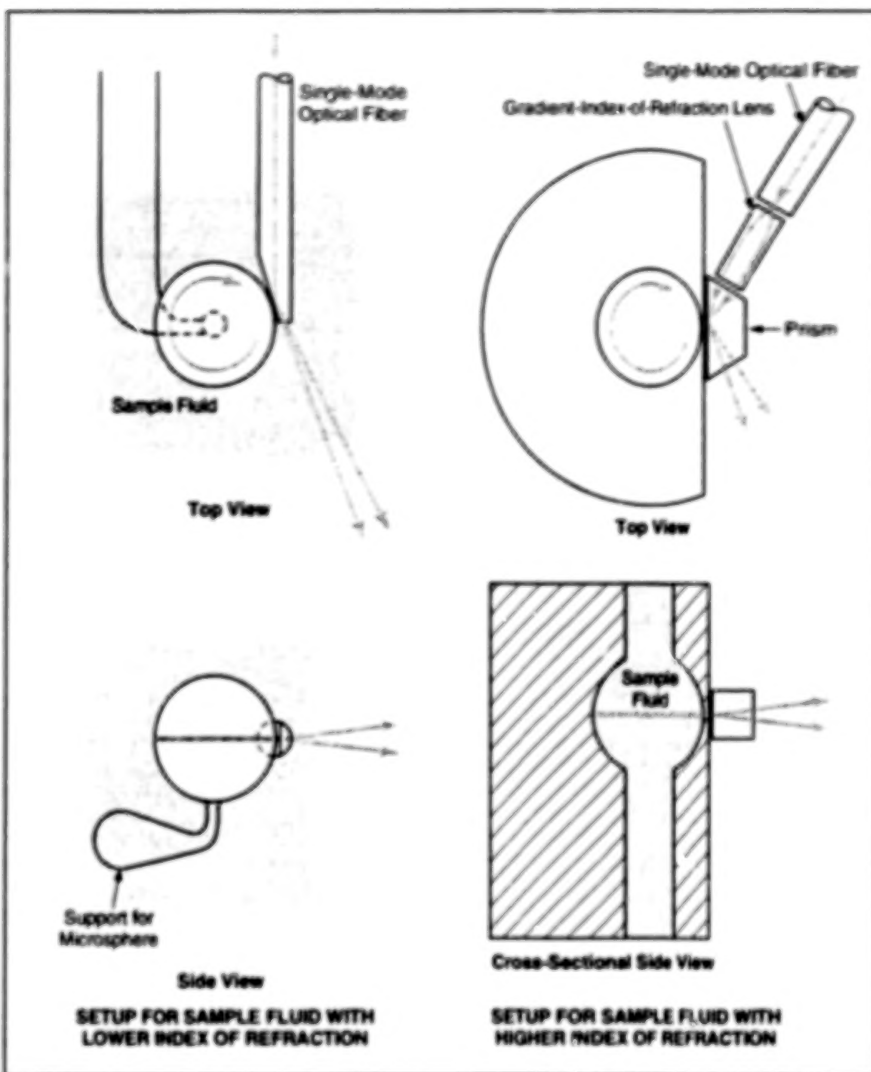
form of a transparent microsphere, (or a microcavity equivalent to a microsphere as described below).

The principle of operation of these sensors is an updated version of that of conventional optical cavity-ringdown spectroscopy (CRDS), wherein resonators in the form of long and bulky Fabry-Perot cavities are used in order to obtain enough effective optical-path length to enable the resolution of small attenuation associated with trace concentrations of analytes. In addition to bulky apparatuses, conventional CRDS requires large samples to fill the Fabry-Perot cavities. In contrast, a microsphere or microcavity sensor of the type under development is designed to be immersed in a sample, which can be small because the microsphere is small. (Alternatively, the sample can be contained in a small cavity as described below.)

The use of transparent microspheres as optical resonators has been reported in a number of prior Tech Brief articles. To recapitulate: In a transparent microsphere, resonance is achieved through glancing-incidence total internal reflection in one or more "whispering-gallery" modes, in which light propagates in equatorial planes near the surface, with integer numbers of wavelengths along nominally closed circumferential trajectories. In the absence of external influences, and assuming that the microsphere is made of a low-loss material, the high degree of confinement of light in whispering-gallery modes results in a high resonance quality factor (high Q).

Suppose that the microsphere is illuminated by laser light at its resonance wavelength and is immersed in a sample liquid or gas that (1) has an index of refraction less than that of the microsphere material and (2) contains a highly diluted chemical species of interest that absorbs light at the resonance wavelength. In that case, the Q of the resonator is diminished through absorption by molecules of that species in the evanescent field of the whispering-gallery modes. Because of the smallness of microspheres (typical diameters from tens to hundreds of optical wavelengths), the smallness of the effective volumes of the evanescent fields (typically 10^{-9} cm^3 or less), and the low level of optical losses intrinsic to microspheres themselves, it is possible to detect very small amounts of optically absorbing chemical species through decreases in Q ; calculations have shown that in some cases, it should be possible to detect amounts as small as single atoms or molecules.

The left side of the figure depicts a typical setup for a microsphere sensor immersed in a sample fluid that has an



A Microspherical Optical Resonator is operated in the presence of a sample fluid that contains an optically absorbing species. The concentration of the species is determined from its effect on the Q of the resonator.

index of refraction less than that of the microsphere. If the index of refraction of the sample fluid exceeds that of a material that could be used to construct a microsphere, then one must use a setup like that shown on the right side of the figure: The sample is contained in a microspherical cavity in a capillary cell made from a transparent material that has an index of refraction less than that of the sample fluid. In this setup, the portion of the sample in the microspherical cavity serves as the whispering-gallery-mode resonator, and coupling between the optical fiber and the microsphere is effected by use of a prism attached to a thin wall that acts as a tunneling (in quantum-mechanical analogy) gap for photons.

The decrease in Q (and thus the amount of the chemical species of interest) can be determined either by measurement of the decrease in the cavity-ringdown time or, if the spectral purity of the laser is adequate,

by traditional measurement of transmission bandwidth. Bandwidth measurement is ordinarily used when Q ranges from $\sim 10^5$ to $\sim 10^6$; cavity-ringdown measurement is more convenient for $Q \gtrsim 10^6$ (typically corresponding to ringdown time $\gtrsim 30 \text{ ns}$). While the precision with which the absolute value of Q can be determined is usually no better than few percent, variations in Q can be measured with greater precision. In state-of-the-art CRDS as performed with Fabry-Perot cavities, it is possible to resolve ringdown times to fractional variations as small as about 2×10^{-3} at data-acquisition rates of about 1 kHz. Hence, it is possible to obtain absorption spectra with satisfactory signal-to-noise ratios even though the losses added by the chemical species of interest may be only small fractions of the intrinsic optical losses of the resonators themselves.

This work was done by Vladimir Itchenko and Lute Maleki of Caltech for

NASA's Jet Propulsion Laboratory
Further information is contained in a TSP [see page 1].

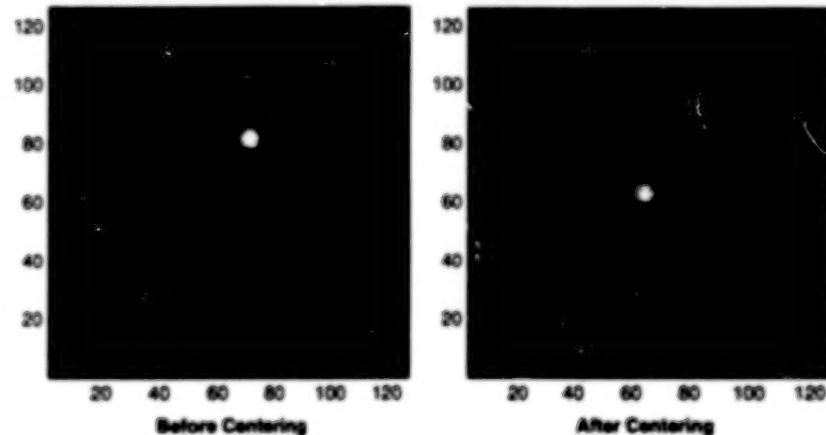
In accordance with Public Law 96-517, the contractor has elected to retain title to this invention. Inquiries concerning

rights for its commercial use should be addressed to
Technology Reporting Office
JPL
Mail Stop 249-103
4800 Oak Grove Drive

Pasadena, CA 91109
(818) 354-2240
Refer to NPO-21061, volume and number of this NASA Tech Briefs issue, and the page number.

Coarse Alignment of a Segmented Telescope Mirror

This method provides for correction of large initial alignment errors.



These Computer-Simulated Pictures show how images of the same star formed by multiple mirror segments might look in a typical case, before and after centering and before any focus or coarse phase adjustment.

A method of coarse alignment has been proposed for a primary telescope mirror that comprises multiple segments mounted on actuators that can be used to tilt and translate the segments to effect wavefront control in increments as fine as a fraction of a wavelength of light. The method was originally intended for application to the Next Generation Space Telescope (NGST), which will have an aperture about 8 m wide and will include nine primary-mirror segments (a central segment and eight outer segments). The method could also be applied to other lightweight telescopes that are similarly designed to rely on active wavefront-control systems instead of traditional massive structures to ensure high optical quality.

A method of coarse alignment is needed because thermal deformations, mechanical loads, manufacturing errors, and other phenomena can give rise to large initial misalignments of the segments; for example, immediately after deployment, the segments of the NGST could be misaligned by

as much as millimeters in piston (displacement along the nominal optical axis) and milliradians in tilt. The present method, to be implemented by the computer that would control the telescope-aiming mechanisms and mirror-segment actuators, provides for reduction of errors in the positions and orientations through the following steps:

1. Aim the telescope at a bright distant point source of light (e.g., a star).
2. Systematically scan the tilts of each mirror segment while repeatedly acquiring star images on an imaging photodetector array at the telescope focal plane. By an algorithm that involves comparison of images with previous images, those images that initially do not fall on the detector can be brought onto the detector and images formed by all the segments can be centered on the detector (see figure).
3. Temporarily tilt the mirror segments to form separated images on the detector. Operating on each image in turn, vary the piston adjustment of the corre-

NASA's Jet Propulsion Laboratory,
Pasadena, California

sponding mirror segment to concentrate as much light as possible into a smaller focal spot of a given size. Repeat the process with a smaller spot size. After a large focus adjustment, recenter the spots according to step 2. Repeat all of the foregoing until the maximum amount of light is concentrated in the smallest possible focal spot.

4. Form a dispersed-fringe sensor as follows: Insert a grism (a right-angle prism with a transmission grating on the hypotenuse face) into the optical path. Tilt all of the outer segments except one to move their images off the detector and to form a dispersed-fringe image by use of the central mirror segment and the remaining outer mirror segment. Analyze the modulation period and orientation of the fringes to determine the magnitude and sign of the piston error between the two segments. Use this error to perform a coarse-phase piston adjustment of the affected outer mirror segment. Repeat this procedure until all of the outer segments have been adjusted.
5. Perform a somewhat finer coarse phase (image-sharpening) adjustment by use of white-light interferometry. Remove the grism from the optical path, then in a manner similar to that of step 4, use the central mirror segment plus one outer mirror segment at a time to form a white-light image of the star. Adjust the outer segment in piston to obtain the highest peak intensity in the image. Repeat the procedure for the remaining outer segments.

This work was done by Scott Basinger, Andrew Lowman, David Redding, and Fang Shi of Caltech and Chuck Bowers of Goddard Space Flight Center for **NASA's Jet Propulsion Laboratory**. Further information is contained in a TSP [see page 1].
NPO-20770

Highly Oblate Microspheroid as an Optical Resonator

Large values of resonance quality factor and finesse have been observed.

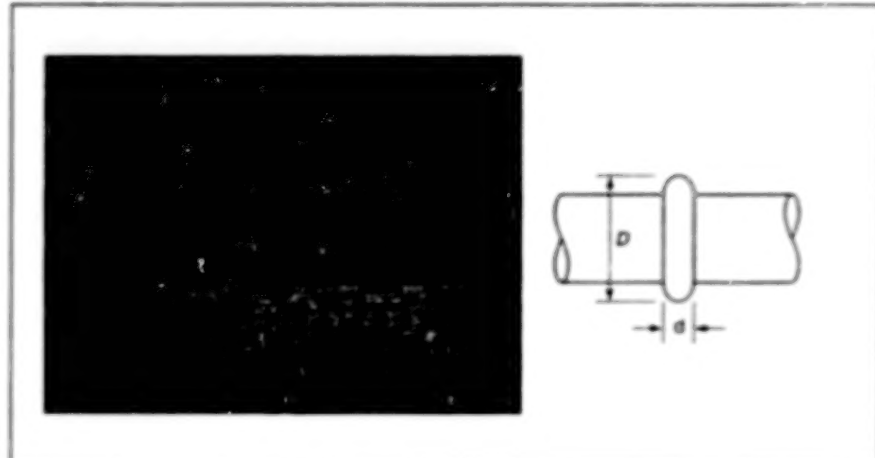
NASA's Jet Propulsion Laboratory,
Pasadena, California

Experiments have shown that a highly oblate microspheroid made of low-dielectric-loss silica glass can function as a high-performance optical resonator. The shape of this resonator (see figure) is intermediate between that of (1) microdisk or microring resonators and (2) microsphere resonators, which have been described in a number of previous *NASA Tech Briefs* articles. As described below, the oblate spheroidal shape results in large values of both resonance quality factor (Q) and finesse. Large values of these parameters are favorable for single-mode operation of a laser or an optoelectronic oscillator.

A microsphere resonator exploits the circulation of light by total internal reflection, in "whispering-gallery" (WG) modes characterized by large values of Q . In contrast, the Q values of microring and microdisk resonators are limited because of significant scattering losses on their flat surfaces.

The preferred WG modes of a microsphere resonator are those in which light circulates by propagating along the equator. As a consequence of spherical symmetry, a microsphere resonator is characterized by a large spectral density of modes because, along with the equatorial modes, some modes with small propagation-vector components transverse to the desired equatorial circulation are also coupled to an input/output device. A large spectral density of modes is not favorable for single-mode operation.

The highly oblate microspheroid resonator is not subject to the disadvantages of microsphere, microdisk, or microring resonators. In the highly oblate microspheroid resonator, the greater curvature of the surface in the direction transverse to the desired equatorial circulation effectively decouples the partly transverse modes from the input/output device. As a result, the resonator can be operated in a regime similar to that of single-longitudinal mode Fabry-Perot etalons. The free spectral range (FSR) [the difference in frequency between successive modes] is defined by



The **Highly Oblate Spheroidal** portion protruding from the cylindrical portion of this object acts as a high-finesse optical resonator. This object was fabricated by heating a sphere of low-loss silica glass to the softening point and squeezing it between flat cleaved tips of an optical fiber.

successive integer numbers of wavelengths packed along the equatorial round-trip light path. For a highly oblate spheroid with an equatorial diameter (corresponding to D in the figure) of the order of hundreds of microns and a typical wavelength of 1.55 μm , an FSR as large as 1 THz is expected; in contrast, for microsphere of approximately equal parameters, the FSR can be expected to be much smaller (typically between 2 and 10 GHz).

At the same time that it affords a much greater FSR, the highly oblate microspheroid resonator retains the high Q (up to about 10^5) typical of microspheres. This high Q corresponds to a resonance bandwidth of a few megahertz. Consequently, the resonator is characterized by very high finesse (finesse = FSR/resonance bandwidth); typical values of finesse range from 10^4 to 10^5 . Heretofore, such high values of finesse were available only in relatively large Fabry-Perot resonators.

If resonators like this one were utilized in simple diode-laser frequency-locking schemes, robust single-mode operation should be possible because the FSRs of the WG modes would be compatible with the gain bandwidth of typical diode

lasers. For spectral-analysis applications, resonators like this one offer a highly attractive combination of miniaturization and unprecedented spectral resolution. For optoelectronic oscillators, resonators of this type could provide convenient sideband frequency references in the terahertz range, provided that appropriate detectors and modulators for this frequency range were also developed.

This work was done by Vladimir Itchenko, X. Steve Yao, and Lute Maleki of Caltech for NASA's Jet Propulsion Laboratory. Further information is contained in a TSP [see page 1].

In accordance with Public Law 96-517, the contractor has elected to retain title to this invention. Inquiries concerning rights for its commercial use should be addressed to

Technology Reporting Office

JPL

Mail Stop 249-103

4800 Oak Grove Drive

Pasadena, CA 91109

(818) 354-2240

Refer to NPO-20951, volume and number of this *NASA Tech Briefs* issue, and the page number.

Books and Reports

Ultralight Balloon Systems for Exploring Uranus and Neptune

A report proposes ultralight balloon systems to carry a 10-kg payload, including

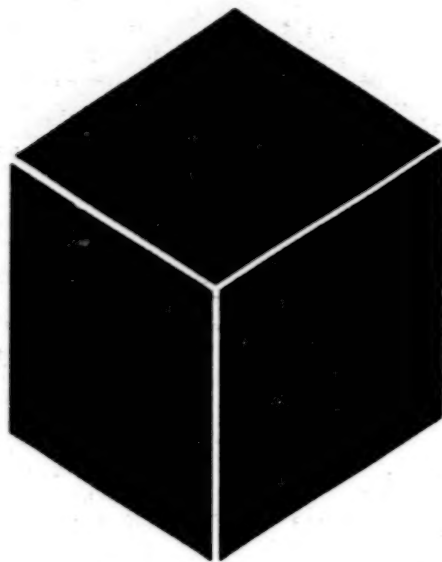
scientific instruments for exploring the atmospheres of Uranus and Neptune. The system masses to be transported to those planets would be kept low by not transporting balloon-inflating gases. Each system would include an upper balloon about

4 m in diameter (0.5 kg) connected via a small port (about 0.25 m in diameter) to a lower balloon about 15 m in diameter (6.4 kg). Through an opening in the lower balloon, the balloons would become filled with low-molecular-weight atmospheric gas

(which has little methane content) during initial descent through the upper atmosphere. At some point in the descent, the opening would be closed. Thereafter, the collected gas would provide buoyancy in the higher-molecular-weight atmosphere (methane content = 2 percent) in the explo-

ration altitude range below the methane-cloud tops, and the lower balloon (used for collection only) would be dropped. The altitude could be held constant or could be regulated by alternately venting gas and dropping ballast, as is done on balloons in the terrestrial atmosphere.

This work was done by Jack A. Jones of Caltech for NASA's Jet Propulsion Laboratory. To obtain a copy of the report, "Ultra Light Balloon for Uranus and Neptune," see TSP's [page 1].
NPO-20543



Materials

Hardware, Techniques, and Processes

- 31 Improvements in Electroformed Copper Alloys
- 32 "Smart Coatings" for In Situ Monitoring of Engine Components
- 32 Ion-Exchange Films for Luminescence Spectrometry of Rare-Earth Ions
- 34 Aggregate-Search Approach for Planning and Scheduling

Books and Reports

- 34 Foaming in Place for Outer-Space Applications

Improvements in Electroformed Copper Alloys

Greater strength and ductility can be obtained by modification of plating conditions.

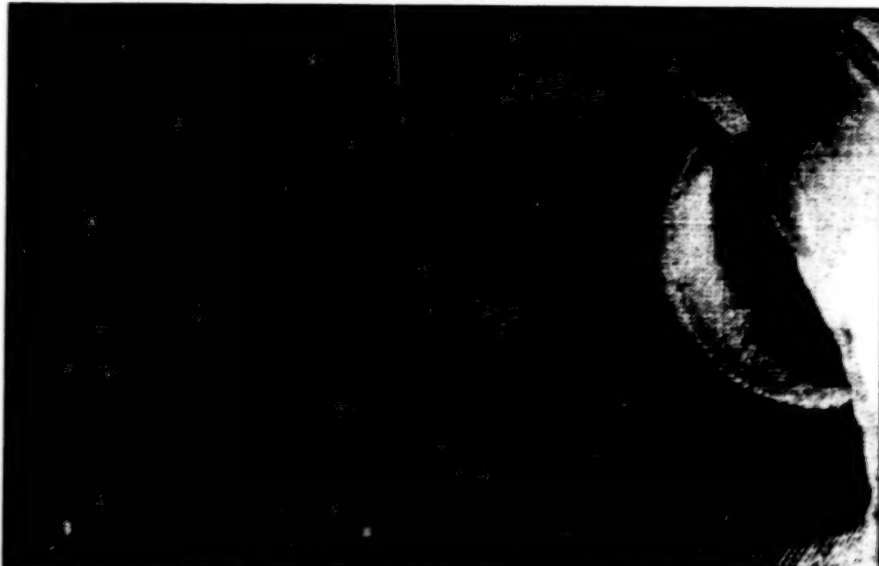
John H. Glenn Research Center,
Cleveland, Ohio

Some success has been achieved in a development program directed toward improving the mechanical properties of electroformed copper-alloy structural components. Typical of such components are bundles of tubes and other heat-exchange devices that have complex shapes. Electroforming of copper alloys is an attractive means for manufacturing such a component because of the high thermal conductivity of copper and because electroforming both produces the alloy and forms the component in nearly net shape in a single process.

Prior to the efforts reported here, electroformed unalloyed copper and copper alloys were found to be too weak for some applications and to lose mechanical strength at moderate operating temperatures. Electroformed nickel — the traditional electroformed structural material — has mechanical properties that are more than adequate for many applications, but its thermal conductivity is less than that of copper. Thus, there is a need to be able to electroform unalloyed or low-alloy copper to obtain high thermal conductivity while producing components strong enough to compete with nickel components at temperatures up to and beyond 200 °C (392 °F). Electroformed copper components could then be used more widely in applications that involve higher temperatures.

The specific objectives and achievements of the program were the following:

- An effort to develop copper or copper alloy electrodeposits having mechanical properties competitive with those of electrodeposited nickel was successful. Although a tensile strength of 689 MPa (100 ksi) was exceeded in limited samples, it was not possible to maintain this level of strength during the long electroforming process times encountered in production facilities. Tensile strengths of 517 to 551 MPa (75 to 80 ksi) accompanied by acceptably large yield strength and ductility were found to be practical in production deposits from an acid copper sulfate bath containing a single proprietary high-molecular-weight organic polymeric additive called "PEG-B." These deposits responded well to heat treatments at temperatures from 149 to 371 °C (300 to 700 °F) and were found to retain yield strengths far higher than that of wrought annealed oxygen-free high-conductivity (OFHC) copper. Unlike



This Tube-Bundle Chamber with a complex shape was fabricated by electrodeposition of copper onto formed copper tubes held in place on a mandrel. No high-temperature joining process was used at any stage of fabrication.

typical acid copper electrodeposits, these materials exhibited acceptably large ductility at elevated temperature.

- An effort to make low-additive, non-alloyed electrolytic copper deposits with yield strengths of at least 49.7 MPa (7.2 ksi) and 10-percent elongation at 371 °C (700 °F) was partially successful: The goals were not achieved at 371 °C (700 °F), but were achieved at 260 °C (500 °F) with deposits from acid copper sulfate baths containing single additives. In each case, the single additive was either chloride ions, xylose, triisopropanolamine, or PEG-B.
- Partial success was achieved in an effort to demonstrate low-alloy-copper deposits with resistance to recrystallization at temperatures up to 500 °C (932 °F) and strengths greater than those of traditional copper deposits. All of these deposits were found to recrystallize to some degree at 371 °C (700 °F). However, after heat treatment at 371 °C (700 °F), deposits from acid bath that contained certain additives exhibited mechanical strengths greater than those of traditional copper deposits; in each case, the additive was either a combination of triisopropanolamine and D+ xylose, a dispersion of submicron-sized α and γ alumina particles, or PEG-B. It was also demonstrated that electrodeposited copper alloyed with a small amount of platinum is a heat-treatable material that exhibits an excellent microstructure after one hour at 371 °C (700 °F), outstanding ductility, and yield strength far greater than that of traditionally electrodeposited copper or wrought annealed copper.
- It was shown that fullerenes could be codeposited with copper to form a dispersion alloy of superior strength with no loss of thermal conductivity. It was also shown that dispersion strengthening could be achieved by codeposition of copper alloys (including copper-platinum alloys) with submicron alumina particles.
- The figure depicts the interior of a tube-bundle thrust chamber (part of a rocket engine) designed and fabricated by electroforming of copper, taking advantage of the developments described above. This is the first tube-bundle thrust chamber made entirely without welding, brazing, or other thermal joining processes; the avoidance of such processes makes it possible to preserve the desired mechanical properties of the copper.

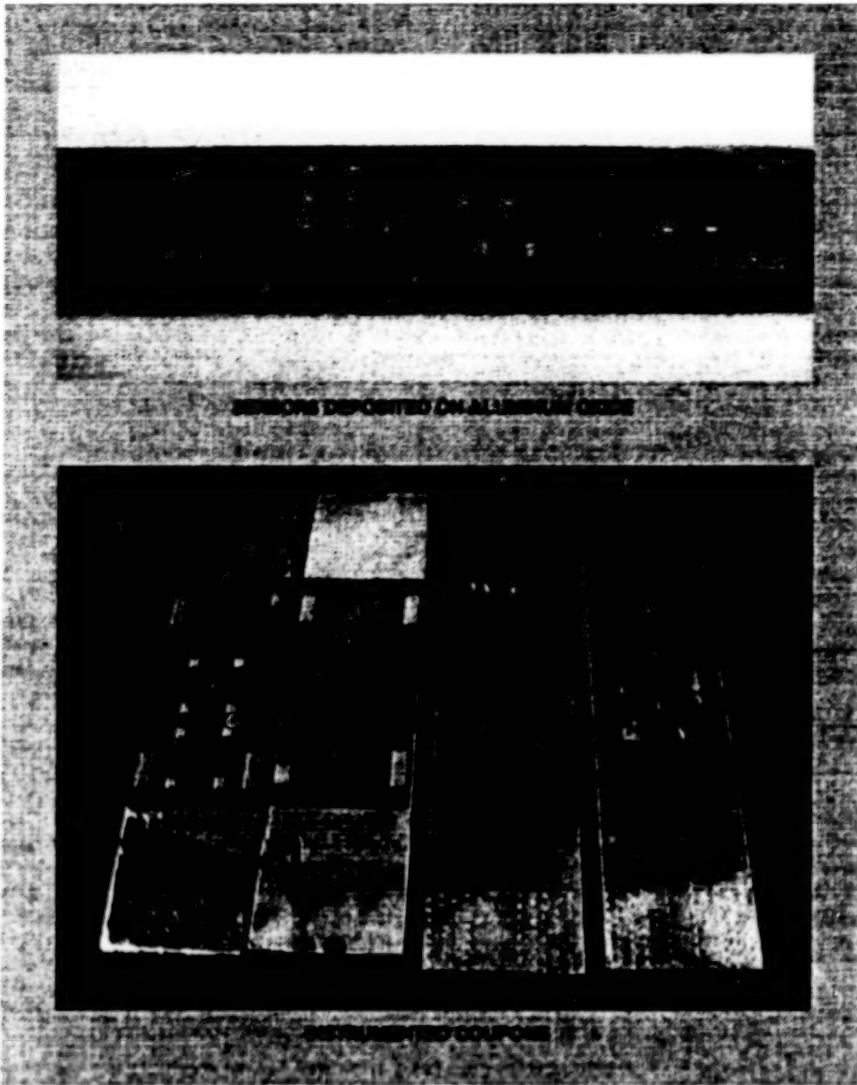
This work was done by G. A. Malone, W. Hudson, B. Babcock, and R. Edwards of Electroformed Nickel, Inc., for Glenn Research Center. Further information is contained in a TSP [see page 1].

Inquiries concerning rights for the commercial use of this invention should be addressed to NASA Glenn Research Center, Commercial Technology Office, Attn: Steve Fedor, Mail Stop 4-8, 21000 Brookpark Road, Cleveland, Ohio 44135. Refer to LEW-16887.

"Smart Coatings" for In Situ Monitoring of Engine Components

Incipient failures could be detected during operation.

John H. Glenn Research Center,
Cleveland, Ohio



"Smart Coatings" containing redundant arrays of eddy-current sensors, crackwires, and capacitive sensors were deposited on nickel-alloy coupons with dimensions of 4 by 1 by 1/8 in. (102 by 25.4 by 3.2 mm).

"Smart coatings" denotes a class of high-temperature-resistant, multilayer, thin (total thickness $< 10 \mu\text{m}$) films, that contain predominantly planar layers of sensor circuitry sandwiched between tough, protective, electrically insulating layers. These films are being developed to enable *in situ* monitoring of aircraft engines during flight

or inspection. "Smart coatings" could be deposited on turbine and compressor blades, turbine-blade hubs, and other critical engine parts to detect incipient failures and other adverse phenomena.

The concept of "smart coatings" incorporates and extends the concept of wireless resonant crackwires, described

in "Resonant Crackwires for *In Situ* Monitoring of Jet Engines" (LEW-16758), *NASA Tech Briefs*, Vol. 24, No. 6 (June 2000), page 8a. Experimental "smart coatings" that have been developed thus far include not only crackwires (for detecting cracks and plastic deformation at instrumented surfaces) but also eddy-current sensors for detecting plastic deformations below the instrumented surfaces, and capacitive sensors for detecting surface contamination (e.g., fuel, ice, or liquid water).

The figure shows some nickel-alloy coupons with experimental "smart coatings." In preparation for fabricating the thin-film sensors, each coupon was ground flat and polished. Each coupon was then coated with an insulating layer of either SiO_2 or Al_2O_3 . Next, thin-film aluminum conductors of sensor circuits were fabricated on the insulating layers by use of photolithographic and deposition techniques and equipment like those used to manufacture integrated circuits.

Tests of coupons containing eddy-current and crackwire sensors have demonstrated that these sensors can detect cracking and plastic deformation. Tests of a capacitance sensor showed that the sensor could detect such surface contaminants as fuel, water, and ice. Tests also revealed that of the two types of sensors for detecting cracks and plastic deformations, crackwires are more practical for use as wireless crack detectors (wireless in the sense that they would be interrogated by radio).

This work was done by Bruce W. McKee, Scott R. Dahl, and Ekaterina Y. Shkarlet of Innovative Dynamics, Inc., for Glenn Research Center.

Inquiries concerning rights for the commercial use of this invention should be addressed to NASA Glenn Research Center, Commercial Technology Office, Attn: Steve Fedor, Mail Stop 4-8, 21000 Brookpark Road, Cleveland, Ohio 44135. Refer to LEW-16919.

Ion-Exchange Films for Luminescence Spectrometry of Rare-Earth Ions

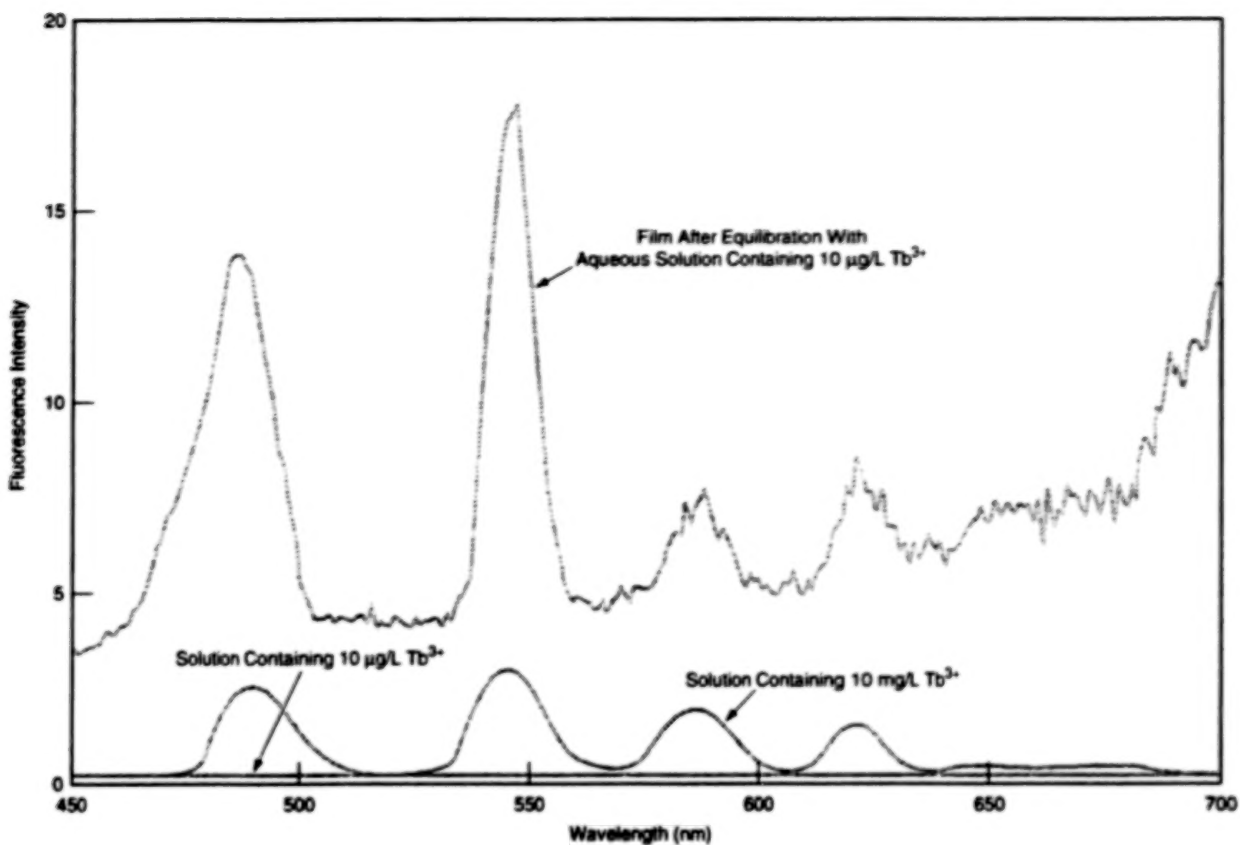
Ions from aqueous solutions are collected in initially transparent films.

Thin, initially transparent films made of variants of a polymeric cation-exchange material have been found to be useful for

facilitating the luminescence detection and quantitation of several rare-earth ions dissolved in aqueous solutions. A film of this

John H. Glenn Research Center,
Cleveland, Ohio

type is prepared in an acid form, then converted to a Ca^{2+} salt form. The acid form of the material consists of polyacrylic acid



Fluorescence Spectra of Tb^{3+} Ions were obtained from aqueous solutions and from an ion-exchange film in which ions had been collected from one of the solutions. At a wavelength of 488 nm, for example, the spectral intensity from the film specimen was 4,100 times that from the corresponding solution. The increase in intensity is a result of both increased concentration and the displacement of coordinated water molecules by carboxylate groups of the ion-exchange material.

entangled in a matrix of insolubilized or further cross-linked polyvinyl alcohol. The conversion to the salt form is effected by exposing the film to $Ca(OH)_2$.

The film is placed in an aqueous solution that one seeks to analyze. By virtue of the cation-exchange function of the film material, rare-earth ions from the solution become concentrated in the film. The film is then mounted in a luminescence spectrometer apparatus for analysis of its rare-earth-ion content by fluorometry and/or phosphorimetry. The concentration of the ions in the film increases the fluorometric and/or phosphorimetric response beyond that achievable through spectrophotometric analysis of the solution (see figure), thereby effectively increasing the sensitivity of measurement of concentrations of the dissolved ions.

This approach to spectrometric analysis is denoted generally as solid-phase spectrophotometry (SPS). As practiced heretofore, SPS has involved (1) the use of ion-exchange resins and (2) the enhancement of selectivity and sensitivity

by use of chromophoric agents as is done in conventional spectroscopy. Unfortunately, many of the ion-exchange resins used heretofore in SPS are not transparent; on the contrary, they are highly absorbing in the spectral regions of interest and are highly scattering at all wavelengths. In contrast, the present ion-exchange films are sufficiently transparent that they do not interfere appreciably with spectrophotometry throughout the visible and most of the ultraviolet spectrum of interest. Furthermore, because the present ion-exchange material is not particulate and its index of refraction matches that of water, the light-scattering problems associated with prior ion-exchange resins are eliminated.

Another advantage arises in connection with fouling by Ca^{2+} ions: These ions, which are often present in natural waters, compete with the metal ions of interest for sites on ion-exchange resins, thus rendering the resin beads less effective. Because it is in the Ca^{2+} form, the present ion-exchange material resists fouling by Ca^{2+} .

One drawback of the present ion-exchange material is that it emits a large amount of background fluorescence. However, this is not a major drawback, inasmuch as the luminescence from the metal ions of interest lasts much longer than does the luminescence from the film; one can suppress the response to the luminescence from the film by use of instrumentation with a temporal-discrimination capability. The only major drawback is slowness of uptake of ions because of the slowness of diffusion of ions to the ion-exchange material.

This work was done by Kenneth W. Street, Jr., of Glenn Research Center and Stephen P. Tanner of the University of West Florida. Further information is contained in a TSP [see page 1].

Inquiries concerning rights for the commercial use of this invention should be addressed to NASA Glenn Research Center, Commercial Technology Office, Attn: Steve Fedor, Mail Stop 4-8, 21000 Brookpark Road, Cleveland, Ohio 44135. Refer to LEW-17074.

Aggregate-Search Approach for Planning and Scheduling

Several algorithms developed for use in automated planning and scheduling of sets of interdependent activities employ aggregation techniques to increase the efficiency of searching for temporal assignments that are legal in the sense that they do not violate constraints. In the aggregate-search approach, one computes the aggregate state and resource requirements of a cluster of interdependent activities and searches for minimally conflicting temporal placements for the corresponding cluster

of requirements. During the search, all activities that temporally constrain each other (for example, as in the requirement to complete activity A before starting activity B) are moved in unison. In computational tests based on a synthetic planning and scheduling problem and on problems from spacecraft and *Rocky-7* Mars Rover operations, the aggregation-search algorithms were found to out-perform alternative algorithms that follow the "naïve" approach of searching for legal placements of the con-

stituent activities individually.

This work was done by Steve Chien, Russell Knight, Gregg Rabideau, and Robert Sherwood of Caltech for NASA's Jet Propulsion Laboratory. Further information is contained in a TSP [see page 1].

This software is available for commercial licensing. Please contact Don Hart of the California Institute of Technology at (818) 393-3425. Refer to NPO-20660.

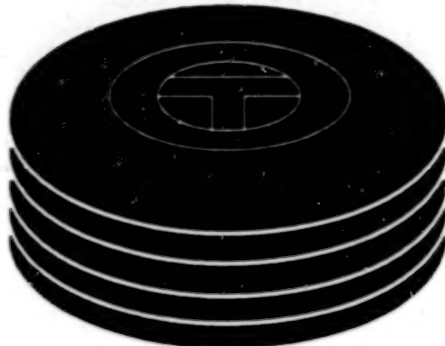
Books and Reports

Foaming in Place for Outer-Space Applications

A report discusses the adaptation of foaming-in-place techniques and materials to outer-space applications. Foaming in place is used commercially in terrestrial sealing, insulating, bonding, and retrofitting applications. The room-temperature outer-

space versions of foaming in place are expected not to differ much from the terrestrial versions, and experiments have confirmed that a commercial two-component liquid polyurethane foaming system could be used on Mars at and near room temperature. However, chemical formulations different from the commercial ones would be needed for foaming at low temperatures.

This work was done by Witold Sokolowski, Andre Yavrouian, and Kerry Nock of Caltech for NASA's Jet Propulsion Laboratory. To obtain a copy of the report, "Foaming-in-Place for Space Applications," see TSP's [page 1]. NPO-21020



Computer Programs

Electronic Systems

37 Software for Analyzing Earth/Spacecraft Radio Interference

Physical Sciences

37 Multithreading Program for Retrieval of Optical Phase Fields

Mathematics and Information Sciences

37 Infrastructure Software for Mining Image Data Bases
37 Software for Generating Mosaics of Astronomical Images
38 Software for Rapid Processing and Display of Earth Data

Computer Programs

Electronic Systems

Software for Analyzing Earth/Spacecraft Radio Interference

The Spectral Analysis Tool (SAT) computer program assists in analysis of interference between radio signals in Earth/spacecraft communications. SAT provides an easy-to-use interactive graphical interface with a menu for selecting among the following utility subprograms: an editor for modulated signal and interference sources of various spectral widths, an editor for inserting an interfering sine wave into the spectrum, a filter editor for simulating effects of a band-limited channel, and a graphics editor for viewing and textual editing of power spectra and spectral-density plots. Also provided are calculators for signal and interference bandwidth and power, plus communication-link-budget tables and interference-analysis tables with choices of antennas, amplifiers, and receivers. The main output of SAT comprises data on interference-to-signal power ratios and system losses with respect to interference-free baseline systems. Optionally, SAT generates color or gray-scale spectral plots or information in textual (including tabular) form on results of power calculations, link-budget parameters, or any other parameter(s) of interest. SAT has been written for execution on a desktop computer running the 3.1, NT, or 95 version of the Windows operating system. The complete SAT software package fits on a standard 3.5-in. (8.89-cm) diskette.

This program was written by K. Oudhiri, K. Angkasa, Leon Truong, E. Kidd, Victor Lo, Mazen Shihabi, F. Chen, J. Rucker, John Gevargiz, and K. Widjono of Caltech for **NASA's Jet Propulsion Laboratory**. Further information is contained in a TSP [see page 1].

This software is available for commercial licensing. Please contact Don Hart of the California Institute of Technology at (818) 393-3425. Refer to NPO-20422.

Physical Sciences

Multithreading Program for Retrieval of Optical Phase Fields

A multithreading computer program performs phase-retrieval and -unwrapping

calculations to extract accurate image phase maps from noisy image magnitude fields generated by adaptive optics. [As used here, "phase retrieval" signifies the calculation of phase map modulo 2π , while "unwrapping" signifies the elimination of the integer-multiple-of- 2π phase ambiguity.] The program includes a MATLAB front-end script integrated with a multi-threaded computing kernel in a set of C routines. The MATLAB script controls the flow of computations and provides a graphical user interface. Major computations are performed in C routines, wherein multiple computing threads are generated to parallelize the computations. The MATLAB script starts the C routines through a function call using MATLAB's MEX interface, and the results of the computations are returned from C routines to the MATLAB script. The program parallelizes the computations whenever multiple central processing units (CPUs) are available; this feature reduces the execution time significantly. Because MATLAB is popular in engineering computing, and increasing numbers of computers are equipped with multiple CPUs and multi-threading software libraries, this program has significance beyond the original adaptive-optics application as an example of how to do high-performance engineering computing at relatively low cost.

This program was written by Scott Basinger, John Lou, and David Redding of Caltech for **NASA's Jet Propulsion Laboratory**. Further information is contained in a TSP [see page 1].

This software is available for commercial licensing. Please contact Don Hart of the California Institute of Technology at (818) 393-3425. Refer to NPO-20848.

Mathematics and Information Sciences

Infrastructure Software for Mining Image Data Bases

Diamond Eye is a computer program that enables a user equipped with only a personal computer, web-browser software, and a network connection to analyze large collections of scientific image data. The system is based on a distributed applet/server architecture that provides platform-independent access to image mining services. A user interacts with the

system through a Java applet interface that is dynamically downloaded when a session is established. There is no need for the user to install "client" software or perform upgrades; the latest stable version of the applet is available automatically. Each server program is typically co-located with a large image repository to enable mining the data in place. Servers are also coupled with an object-oriented data base and a computational engine such as a network of high-performance workstations. The data base provides persistent storage and enables querying of the "mined" information. The computational engine provides parallel execution of the most demanding parts of the data-mining task: image processing, object recognition, and querying-by-content operations. Diamond Eye is currently being used to locate and catalog geological objects in large image collections, but the design provides infrastructure for a range of scientific-data-mining applications. The system can be easily extended to incorporate domain-specific algorithms in any executable form (translation to the Java language is unnecessary).

This program was written by Michael Burl, Charles Fowlkes, Saleem Mukhtar, Joseph Roden, and Andre Stechert of Caltech for **NASA's Jet Propulsion Laboratory**. Further information is contained in a TSP [see page 1].

In accordance with Public Law 96-517, the contractor has elected to retain title to this invention. Inquiries concerning rights for its commercial use should be addressed to

Technology Reporting Office
JPL
Mail Stop 249-103
4800 Oak Grove Drive
Pasadena, CA 91109
(818) 354-2240

Refer to NPO-20921, volume and number of this NASA Tech Briefs issue, and the page number.

Software for Generating Mosaics of Astronomical Images

Software is being developed to "stitch" together multiple astronomical images of small, adjacent patches of the sky into a single mosaic image of a large portion of the sky. These mosaics make data from large areas of the sky readily available for efficient viewing of many types of celestial objects and large-scale structure in the sky.

that is not apparent on a smaller scale. This software can be run on both single-processor computers and multiprocessor systems. The input patch image data can be of any type, resolution, coordinate system, and projection consistent with the Flexible Image Transport System (FITS), which is a commonly used astronomical data format. The software uses information in FITS headers to reproject the input image data into a common coordinate system and then to translate the data into the output mosaic at a resolution and in a coordinate system specified by the user. This software is part of a "Virtual Observatory" system being developed for analysis and display of astronomical images and catalogs.

This program was written by Joseph Jacob of Caltech for NASA's Jet Propulsion Laboratory. Further information is contained in a TSP [see page 1].

This software is available for commercial licensing. Please contact Don Hart of the California Institute of Technology at (818) 393-3425. Refer to NPO-21121.

Software for Rapid Processing and Display of Earth Data

Digital Earth Workbench is a computer program that facilitates retrieval of Earth-related imagery and viewing of the imagery on either an ordinary computer video screen or a virtual-reality (head-

tracked stereoscopic) display system. Examples of imagery that can be processed by this software include (but are not limited to) high-resolution topography, photographic images, maps, and images synthesized from geophysical data. Image data can be retrieved from storage at remote sites. The user can easily navigate to the data pertinent to any location on Earth and browse through imagery for that location. For images that are not topographical, the user can view the images overlaid on high-resolution Earth topography.

The development of Digital Earth Workbench was prompted by a desire for a system that is simple enough for use by a child and powerful enough to be useful to a scientist and that, in comparison with similar prior software, offers faster processing of image data and better performance as a virtual-reality interface. Digital Earth Workbench incorporates software components that exploit the capabilities of advanced computer hardware, mediate the exchange of data with virtual-reality display systems, implement advanced rendering concepts, and generate real-time graphical displays. These components are integrated in such a way as to focus them on displaying Earth-science data. The virtual-reality components of this software are particularly valuable because they provide an easy-to-use interface for obtaining three-dimensional-appearing

views of data in relation to the Earth.

In this software, the topography of the entire surface of the Earth is divided into tiles. Each tile is further divided into subtiles. Each tile and subtitle provide representations of the topography at several different levels of detail. As the user roams through geographically indexed data, the appropriate tiles, subtiles, and level of detail of each are selected on the basis of their proximity to the location selected by the user: this selection scheme limits the amount of graphical information that must be processed, so that the frame rate can remain high.

For overlaying images on Earth topography (and/or on a corresponding base Earth image), the software utilizes a multipass rendering mechanism. After the components of an overlay have been set up, the topography is redrawn, using the overlay information as texture superimposed on the topography. The redrawing process is limited to the largest topographical tile or subtitle needed to encompass the overlay, in order to minimize the amount of geometrical information that must be processed. Multiple overlays are blended by use of common translucency techniques.

This work was done by Stephen Maher of Goddard Space Flight Center. Further information is contained in a TSP [see page 1].

GSC 14263



Mechanics

Hardware, Techniques, and Processes

- 41 Estimation of Wheel-Contact State of a Robotic Vehicle
- 41 Controlling Speed of a Robotic Vehicle Over Rough Terrain
- 42 Advanced, Lightweight, Low-Power-Consumption Actuator Brake

Books and Reports

- 43 Stable Microwave-Beam-Riding Spacecraft

40 BLANK PAGE

Estimation of Wheel-Contact State of a Robotic Vehicle

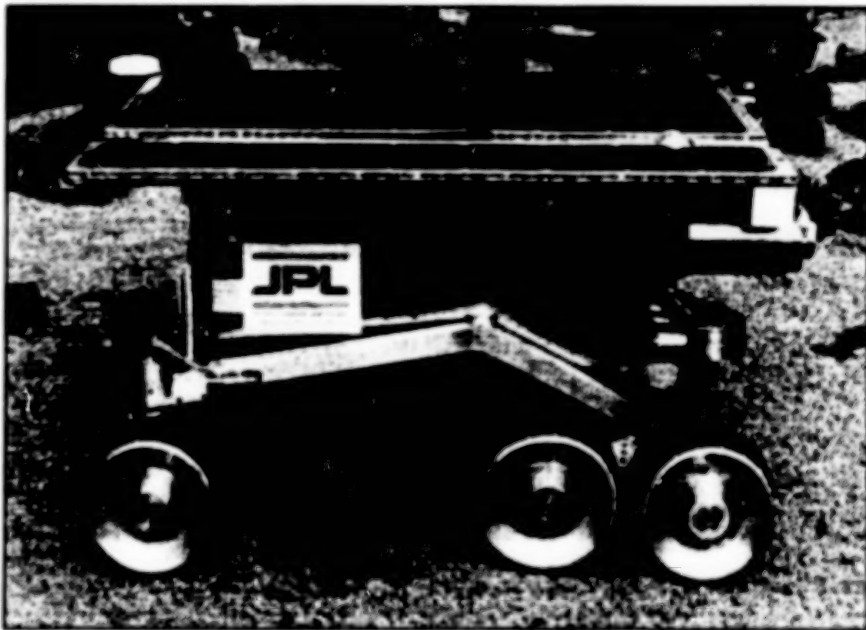
An odometric estimate of position can be made more accurate.

NASA's Jet Propulsion Laboratory,
Pasadena, California

A method of estimating the state of contact between (1) the wheels of a robotic vehicle equipped with a rocker-bogey suspension and (2) the ground has been devised. The contact-state information is used to estimate the position of the vehicle with an accuracy greater than that achievable by simple odometry and inertial sensing when the vehicle moves over undulating or bumpy terrain under conditions in which processing of visual odometry information is infeasible or undesirable. The contact-state information can also be used to increase understanding of those aspects of design and operation of the vehicle that affect stability and traction, as affected by the configuration of the rocker-bogey and steering mechanisms. The method in its original form is meant to be applied to Rocky-7 (see figure) — a "rover"-type vehicle used in research on robotic-vehicle concepts for the exploration of Mars. The method is also potentially applicable to terrestrial robotic vehicles that could be used in field operations in agriculture, mining, and other industries.

In this method, the forward kinematics of the vehicle (proceeding from the vehicle frame to the wheel/ground contact points) are embedded within a constraint that is treated as a measurement. The forward kinematic chain velocity for each wheel includes a component defined by the sequence of links that join the vehicle frame to the wheel/ground contact point, plus a component given by the slip between the wheel and the ground. An important element of the method is the notion of a slip measurement or constraint that defines the six-degree-of-freedom (6-dof) motion of the contact frame on the wheel, relative to the ground. The slip is a function of the vehicle configuration, the 6-dof vehicle velocity, the location of the wheel/ground contact points, and the rates of rotation of the joints along the various kinematic chains.

The slip can be decomposed into a



Rocky-7 includes a rocker-bogey suspension with two steerable front wheels. The present method provides for estimation of the state of wheel/ground contact on the basis of sensor readings and the highly nonlinear kinematics of the rocker/bogey suspension.

deterministic component and a component that is known in a statistical sense only. The deterministic component of the slip is used to capture the effects of a known steering action; for example, a known rotational slip about the vertical is always present at each wheel to accommodate the yaw motion of the vehicle during a turn. Also, some transverse slip is introduced because of the nature of the nonsteered bogey wheels. These deterministic slips are easily calculable for steered motions on flat ground, and those calculated for flat ground are used as approximations for those on nonflat ground. Other slip constraints can be derived from experiments. Slips that are modeled statistically include those attributable to wheel-ground interactions and to curvature of the terrain.

The state-estimation algorithm of this method utilizes an extended Kalman filter to fuse data from multiple sensors aboard

the vehicle (e.g., a gyroscope, a Sun sensor, and accelerometers) while taking account of the kinematics of the rocker-bogey suspension and steering. In addition to the kinematic elements described above, the extended Kalman filter incorporates process models of attitude, translation, gyroscope bias, plus observation models for the gyroscope, Sun sensor, and accelerometer. The highly nonlinear kinematics of the rocker-bogey suspension and the wheel/ground contact points are incorporated into the filter via the slip constraint. The algorithm exploits the ability of the Kalman filter to perform the appropriate least-squares averaging of the action of each kinematic chain in the vehicle.

This work was done by J. Balaram of Caltech for **NASA's Jet Propulsion Laboratory**. Further information is contained in a TSP [see page 1].
NPO-20960

Controlling Speed of a Robotic Vehicle Over Rough Terrain

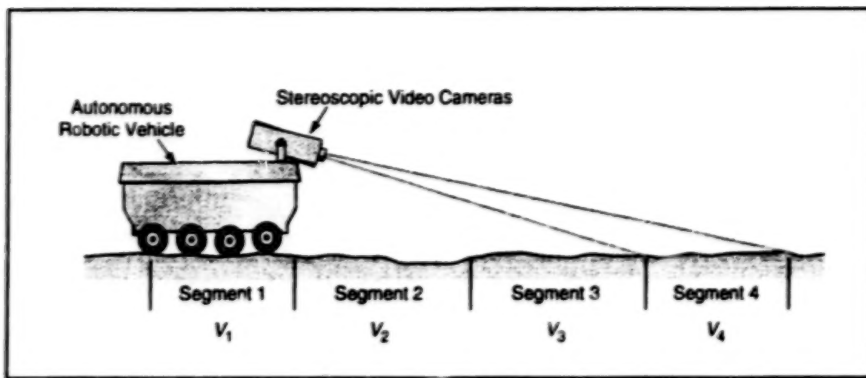
Speed is commanded according to vehicle dynamics and stereoscopically measured terrain-height variations.

NASA's Jet Propulsion Laboratory,
Pasadena, California

A method of computing the speed at which to command an autonomous robotic vehicle to travel over rough terrain has

been devised. The method amounts to a robotic implementation of the practice in which, during approach to a visibly rough

surface, a human driver intuitively reduces the speed of a car or truck to prevent excessive bounce, damage to the vehicle,



Maximum Allowable Speeds are calculated for four path segments on the basis of terrain-height variations computed from stereoscopic images of the terrain ahead. At any given time, the commanded speed of the vehicle along the path is the minimum of V_1 through V_4 .

or loss of control.

The method is applicable to a robotic vehicle equipped with (1) a stereoscopic machine-vision system that generates data equivalent to a topographical map of the terrain in the vicinity of the vehicle, (2) an onboard navigation system that computes the planned path of the vehicle across the terrain, and (3) a speed-control system. In this method, the process for generating a speed command begins with utilization of the topographical and planned-path data to compute the relative surface height as a function of distance along the planned tire tracks immediately ahead of the vehicle. The roughness of the surface along each tire track is quantified in terms of the derivatives (particularly the second derivative) of surface height with respect to distance. To suppress the additional noise that would

otherwise be generated by differentiation of noisy height data, the height-vs.-distance data are fitted piecewise cubic spline polynomial curves, the parameters of which give the required derivatives directly.

The maximum allowable speed, for the purpose of generating a velocity command, is deemed to be the speed that results in a maximum allowable bounce (as quantified in terms of vertical acceleration). To calculate vertical acceleration, the dynamics of the vehicle at each tire are represented by a mathematical model in which a spring-and-damper combination (representing the tire) is in series with another spring-and-damper combination (representing the suspension mechanism) that supports a rigid mass equal to a portion of the mass of the vehicle. Analysis of this model leads to a quadratic equation for the maximum allowable

speed as a function of the maximum allowable vertical acceleration and of "road forcing" terms that contain the second derivative of the surface height. The solution of this equation for each position along a tire track yields the maximum allowable speed for that position.

Of course, it is necessary to (1) decelerate the vehicle to the maximum allowable speed for a given rough spot at least some short time before the vehicle reaches that spot, and (2) keep the speed low until the vehicle has cleared the rough spot. One strategy to accomplish this involves (1) maintaining a sequence of allowable speeds computed for nonoverlapping segments of the vehicle path immediately ahead and (2) commanding, at any given time, a speed that is the minimum of these allowable speeds. For example, suppose that four maximum-speed values (V_1 through V_4) are sufficient and that they pertain to segments of the path from the rear wheels to the stopping distance in front (see figure). As the vehicle moves forward, the current value of V_1 is dropped from the sequence, the current values of V_2 through V_4 are assigned to V_1 through V_3 , respectively, and a new maximum speed V_4 is computed for the new fourth path segment coming into view.

This work was done by Kenneth D. Owans of Caltech for NASA's Jet Propulsion Laboratory. Further information is contained in a TSP [see page 1].
NPO-20762

Advanced, Lightweight, Low-Power-Consumption Actuator Brake

This brake features a modular, fault-tolerant design.

Lyndon B. Johnson Space Center,
Houston, Texas

Parameter	Standard Practice	NASA Design
Torque + Weight, lb·ft/lb	1.6	5.2
Volume, in. ³	28.5	12
Response Time, ms	40	20
Power Consumption, W	0.5	0.012 (Conservative Estimate)

Key Parameters of the NASA design are compared with those of a design according to standard practice.

An advanced, lightweight, low-power consumption brake has been developed to satisfy NASA's special requirements for use on actuators during spaceflight. This

brake can increase the stopping, holding, and parking ability of a spacecraft while reducing its electrical power consumption. Two notable strengths of the design

of this brake are modularity and fault tolerance. The use of brakes like this one can be expected to increase performance measures and safety margins in terrestrial as well as outer-space applications.

Brakes of this type are used in outer space or on Earth to stop, hold, or park a moving vehicle that is being driven by electromechanical devices. In spaceflight, brakes must be lightweight, exhibit short closing times, and conform to the geometries of pre-existing actuator structures. The principal issue in designing brakes for spacecraft is excessive power consumption, which is particularly costly under circumstances in which resources are already at a premium and the loss of resources could cost time or jeopardize human lives. Although in some respects the situation is less critical on Earth, lives

are nonetheless frequently lost when vehicle brakes fail. An advanced electro-mechanical braking system that satisfies the requirements for spacecraft and that increases the braking ability of Earth vehicles would surely prove beneficial to the government and to commerce.

When NASA assigned the task of designing an advanced braking system that could reduce the cost of spaceflight, it asked not only that the essential requirements pertaining to spaceflight (low power consumption and minimal thermal effects) be satisfied but that they be satisfied in a manner surpassing previous designs while

reducing power consumption to 1/100 of a baseline level. Some of the benefits of the NASA design, relative to a design according to standard practice, are illustrated in the table. The modularity of design is another benefit: two or more modules can be included in a single braking system, so that if one brake fails the other brake(s) will continue to operate. Such redundancy creates a level of fault tolerance unequalled in previous space-deployed brake designs.

Brakes like this one could be used not only in outer space but also on Earth in applications in which multiple actuators

operate at moderate to high temperatures, design goals include minimization of weight and power consumption, and there is a need for the insurance added by redundancy. Such brakes would be suitable for use with servo-actuators, especially in robots, wheeled exploratory vehicles, antenna-deployment mechanisms, and power tools.

This work was done by Delbert Tesar, Hau Nguyen-Phuc Pham, Derak Black, William F. Weldon, Richard Hooper, and Michael James Meaney of the University of Texas at Austin for Johnson Space Center.

MSC-22867

Books and Reports

Stable Microwave-Beam-Riding Spacecraft

The work considers passive dynamic stability of sail craft, propelled by microwave beams. Such systems are under consideration as low-cost means of interstellar travel. Sail-craft shapes offering passive dynamic (neutral) stability are identified. Passive stability is a key mission-enabling attribute. Very large, umbrellalike structures made of strong, lightweight

materials, such as carbon-fibers, attached aft of the payload can provide sufficient propulsive power by reflecting incident microwave energy. Not all reflector shapes are stable however. The key contribution of this work is the identification of reflector shapes which possess passive dynamic stability in translation and attitude. Reflector substructure must be concave to incident radiation and must be located aft of the vehicle center of gravity, c.g. (i.e., the incident radiation encounters c.g. first).

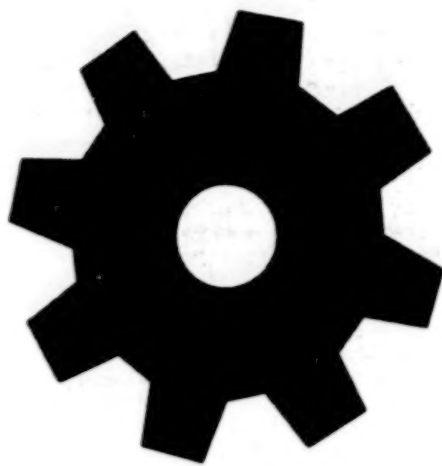
Critical parameters for passive dynamic stability are identified. A simulation/analysis tool is also developed which can be used to adequately address the stability issue of other potential sail-craft configurations.

This work was performed by Gurkirpal Singh of Caltech for NASA's Jet Propulsion Laboratory. To obtain a copy of the report, "Stable Microwave Beam-Riders," see TSP's [page 1].

NPO-21035

44

BLANK PAGE



Machinery

Hardware, Techniques, and Processes

- 47 Tooling for Controlled Grinding of an Edge To Remove Defects
- 48 Dynamic Balancing of Multiple Independent Stirling Engines
- 49 Using Artificial Neural Networks To Monitor Stirling Engines

46

BLANK PAGE

Tooling for Controlled Grinding of an Edge To Remove Defects

Worker fatigue, process time, and risk of scrapping expensive workpieces are reduced.

Marshall Space Flight Center,
Alabama

A special-purpose grinding tool and fixtures have been developed for reworking an edge of a seal surface on a nozzle-throat-support housing in a rocket engine (see Figure 1) to remove defects caused by corrosion. Although the design of the tooling is specific to the original rocket-engine application, some aspects of the design may stimulate thinking about solutions to other special machining problems that cannot be solved readily by use of standard tooling alone.

According to the engineering specification that governs the rework of the seal surface, the radial depth of edge material removed must not exceed 0.032 in. (0.81 mm). Previously, the rework involved the manual filing of the edge. The filing procedure was difficult to control; the maximum allowable depth was sometimes exceeded, making it necessary to scrap the housing. The present tooling was developed to provide greater accuracy and reliability in reworking the seal surface and to prevent removal of edge material beyond the maximum allowable radial depth.

The tooling (see Figure 2) includes a base fixture equipped with indexing bearings that ride along datum surfaces of the throat-support housing. The base is secured to the housing by spring-loaded pincher bearings on the inside and a spring-loaded pivot bearing on the outside. An adjustable outrigger bearing adds stability and provides for alignment of the index bearings. Two precise linear shafts that have been press-fit into the base fixture serve as supports and guides for the grinding tool.

The grinding tool is an automotive valve-seat grinding stone on the shaft of a low-speed air motor. A cradle that is positioned between the two shafts and that rides along the shafts on bushing bearings holds the motor at the angle needed to enforce the correct alignment of the grinding stone with the surface of the workpiece.

A micrometer on the base fixture is used to adjust the position of a hard stop that limits the depth of grinding; this adjustment is performed before grinding. During grinding, a technician applies gentle, radially outward force to the cradle while moving the base fixture circumferentially to make a smooth transition to the workpiece surface adjacent to the defect to be removed.

In addition to providing better control

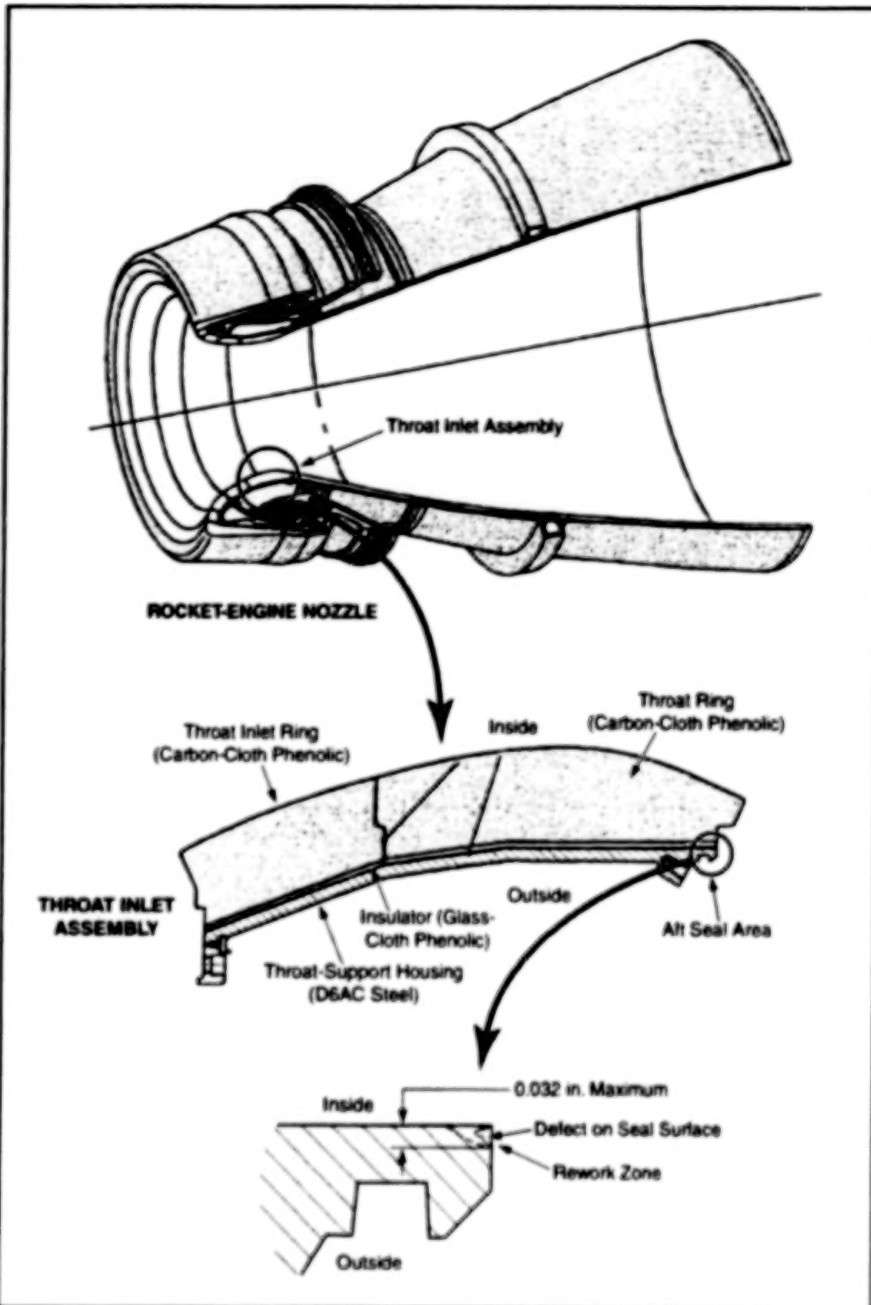


Figure 1. Material Containing a Defect must be removed from the inside edge of the seal surface. The depth of removal must not exceed 0.032 in. (0.81 mm).

over the material-removal process, this tooling saves time and relieves technicians of the tedious and fatiguing filing task. Unlike in manual filing, the technician need not exert major force while stroking. For a typical housing, manual filing takes about ten hours. With the present grinding tool and fixtures, the process can be completed in less than one hour.

This work was done by Ronald B. Montgomery, M. Bryan Ream, and Brent A. Mecham of Thiokol Corp. for **Marshall Space Flight Center**.

MFS-31326

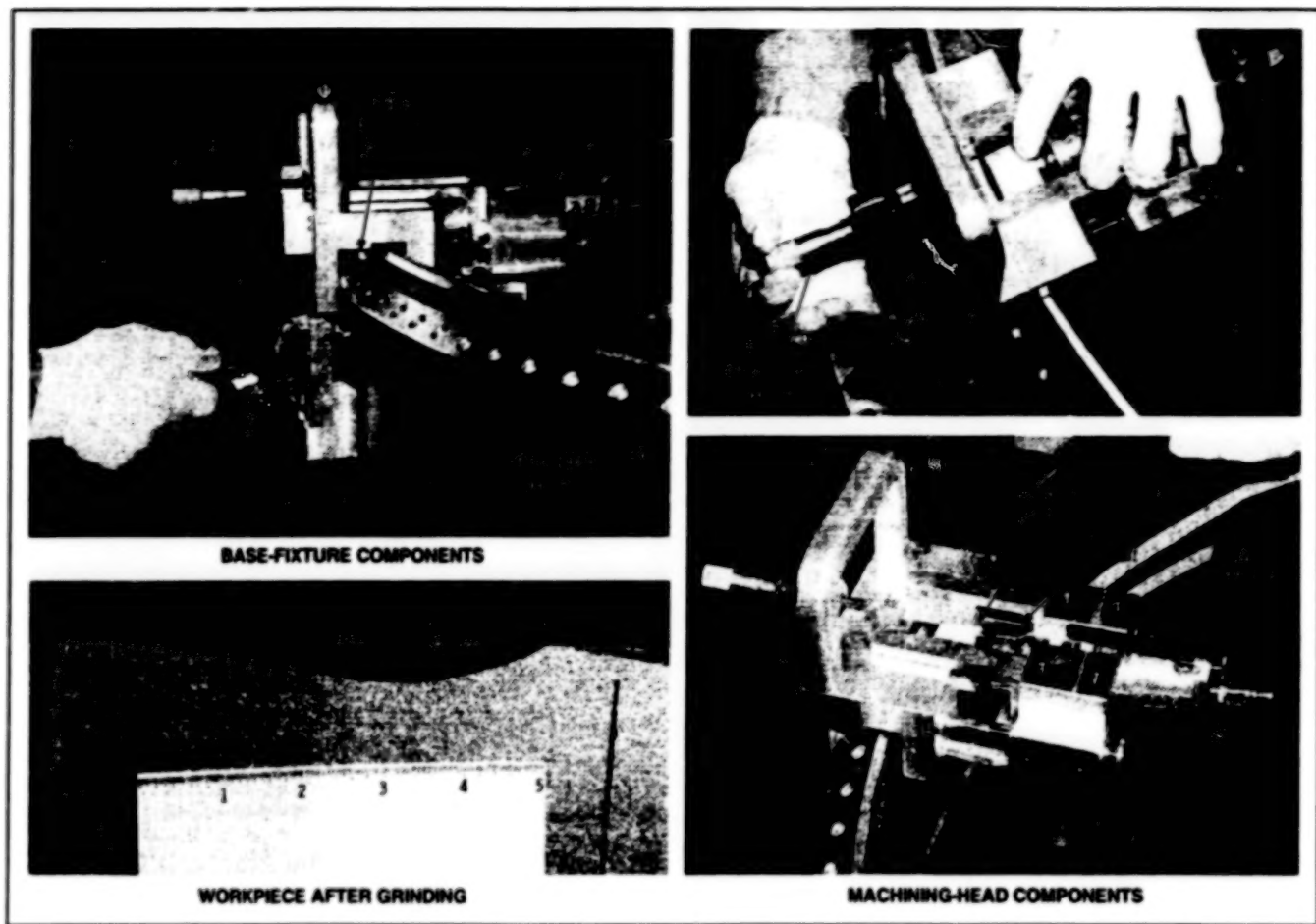


Figure 2. The Grinding Tool and Fixtures make the material-removal process faster, easier, and more controllable, in comparison with a formerly used manual filing process.

Dynamic Balancing of Multiple Independent Stirling Engines

Vibrations are minimized without sacrificing redundancy.

Experiments have shown that an assembly of multiple free-piston Stirling engines can be designed and constructed in such a way as to both (1) make the vibrations of the engines balance each other to minimize the overall level of vibration, and (2) enable the engines to operate independently of each other, so that if one fails, the other(s) can continue to provide power. Prior to these experiments and to the research and development effort that preceded them, it was not possible to achieve both redundancy and suppression of vibrations: The only previously demonstrated method to balance out vibrations of multiple Stirling engines was by use of counter-oscillating pistons coupled to each other via a common thermodynamic hot space, with the engines driving linear alternators connected electrically in series. This older scheme precludes redundancy because the common thermodynamic interaction and the series electrical connection causes

both engines to fail when one fails.

In the present scheme, the multiple Stirling engines in a given assembly are thermodynamically independent of each other. For coupling of vibrations between the engines, the housings of the engines are rigidly connected to each other at their cold ends in an opposed arrangement (see figure). A tuning capacitor is connected in series with the linear alternator of each engine to compensate for the alternator inductance in order to obtain a near unity power factor.

The experiments were performed on a two-engine assembly operating at a frequency =60 Hz and output-power levels ≤ 250 W per engine. When the electrical outputs of the engines were ac-coupled in parallel downstream of the tuning capacitors, the net vibration level was reduced to as little as 1/50 of that of a single engine operating alone. (DC coupling was found to exert no effect on vibrations.) It was

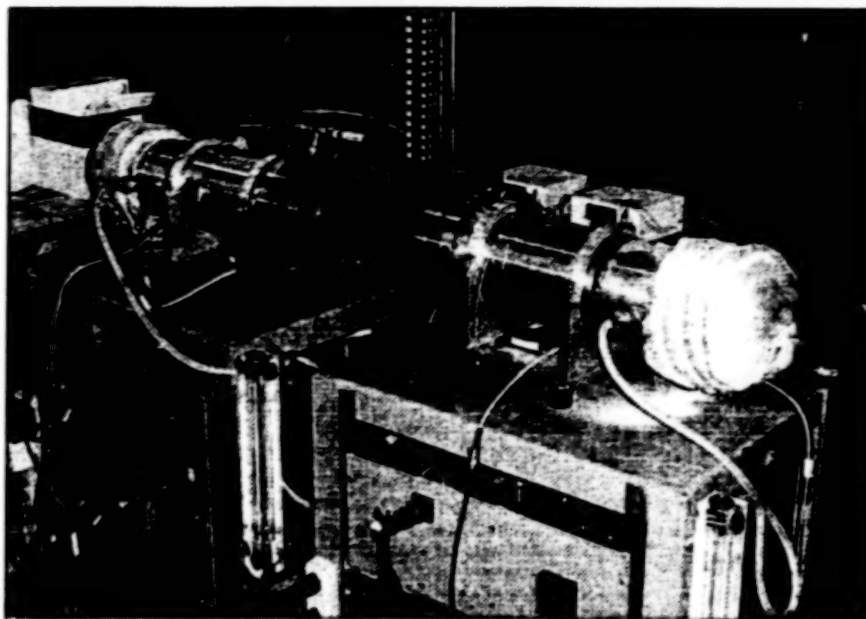
John H. Glenn Research Center,
Cleveland, Ohio

observed that the ac connection between the two engines can be opened or closed at will with no adverse consequences other than that when the connection is opened, the engines gradually drift out of synchronization and thus vibrations are no longer suppressed.

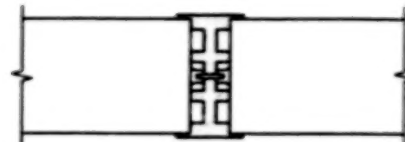
When the ac connection is closed after having been open, the engines come back into synchronization with opposing piston motions, so that vibrations are once again suppressed. When so synchronized, the engines remain synchronized even in the presence of wide variations in charge pressure or hot-end temperature of one engine relative to the other. No significant transient overstrokes or other potentially damaging behavior was observed.

This work was done by Maurice A. White, Laurence B. Penswick, and Songgang Qiu of Stirling Technology Co. for Glenn Research Center.

Inquiries concerning rights for the com-



Stirling Engines Synchronized for System Operation With Low Vibrations



Two Engines

mercial use of this invention should be addressed to NASA Glenn Research Center, Commercial Technology Office, Attn: Steve Fedor, Mail Stop 4-8, 21000 Brookpark Road, Cleveland, Ohio 44135. Refer to LEW-16823.

Housings of Multiple Free-Piston Stirling Engines are rigidly connected at their cold ends so that vibrations are coupled among them. The arrangement is symmetrical so that their piston motions will balance if properly synchronized. Experiments have shown that synchronization is achieved when the engine electrical outputs are ac-coupled.

Using Artificial Neural Networks To Monitor Stirling Engines

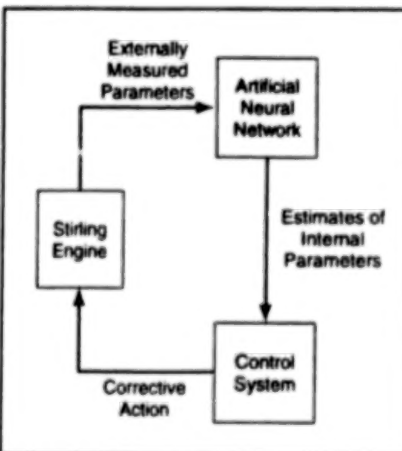
Minimal, noninvasive instrumentation can be used.

An important secondary topic addressed in the research and development effort described in the preceding article is the use of artificial neural networks to improve the monitoring and thus the control and safety of multiple free-piston Stirling engines. Information collected by monitoring subsystems constitutes essential feedback for use by control and safety subsystems. This information includes such externally measurable quantities as heater-head temperatures, motions of engine housings, and output currents and voltages.

Prior to this effort, typical approaches to the monitoring and control of Stirling engines involved the use of extensive data-acquisition systems that collected, in addition to externally measurable quantities, such critical internal operating parameters as pressures and motions of components as measured by invasive pressure and position probes, respectively. Unfortunately, such probes are expensive, are potential sources of failure, and compromise design options.

The neural-network approach offers an inexpensive, simple, and highly reliable

John H. Glenn Research Center, Cleveland, Ohio



An **Artificial Neural Network** could be part of the feedback control system of a Stirling engine or an assembly of such engines. The neural network would estimate internal operating parameters (e.g., pressure or piston motions) from externally measurable quantities (e.g., output current, output voltage, and current/voltage phase angle).

alternative to the use of invasive probes. An artificial neural network can be particularly useful for modeling and monitoring a

complex mechanical/electrical system like a Stirling engine, for which the mathematical relationships among input and output variables are either unknown or too complex to be represented by an analytical model. The basic idea is to train an artificial neural network to infer information about internal operating conditions from measurements by minimal (only external) instrumentation in order to detect actual or incipient failure or deterioration.

An autonomous control system could process the output of such a neural network (see figure) into control commands to perform corrective actions to maintain reliable engine operation. For example, in the case of two or more Stirling engines operating in synchronization as described in the preceding article, a neural network could compensate for deterioration of one of the engines by triggering a command to ramp down the output of that engine and ramp up the output(s) of the other engines. The feasibility of this neural-network concept was demonstrated in an experiment on two coupled Stirling engines: While one engine was operated under nominal condi-

tions, the other was operated at a series of reduced pressures to simulate the effects of a slow leak. An artificial neural network, fed only data on root-mean-square currents, output power, and current/voltage phase angles from the two engines was found to infer the decrease in pressure in

the affected engine with high accuracy.

This work was done by Laurence B. Penswick of Stirling Technology Co. for Glenn Research Center. Further information is contained in a TSP [see page 1].

Inquiries concerning rights for the commercial use of this invention should be

addressed to NASA Glenn Research Center, Commercial Technology Office, Attn: Steve Fedor, Mail Stop 4-8, 21000 Brookpark Road, Cleveland, Ohio 44135. Refer to LEW-16822.



Mathematics and Information Sciences

Hardware, Techniques, and Processes

- 53 Algorithms for Recognition of Objects in Color Stereo Images
- 54 Expert System Controls and Monitors Thermal System
- 55 Cascade Error-Projection Learning in Neural Networks
- 55 A Metric for Visual Quality of Digital Video

52

BLANK PAGE

Algorithms for Recognition of Objects in Color Stereo Images

Objects of known size, shape, and color can be recognized in real time.

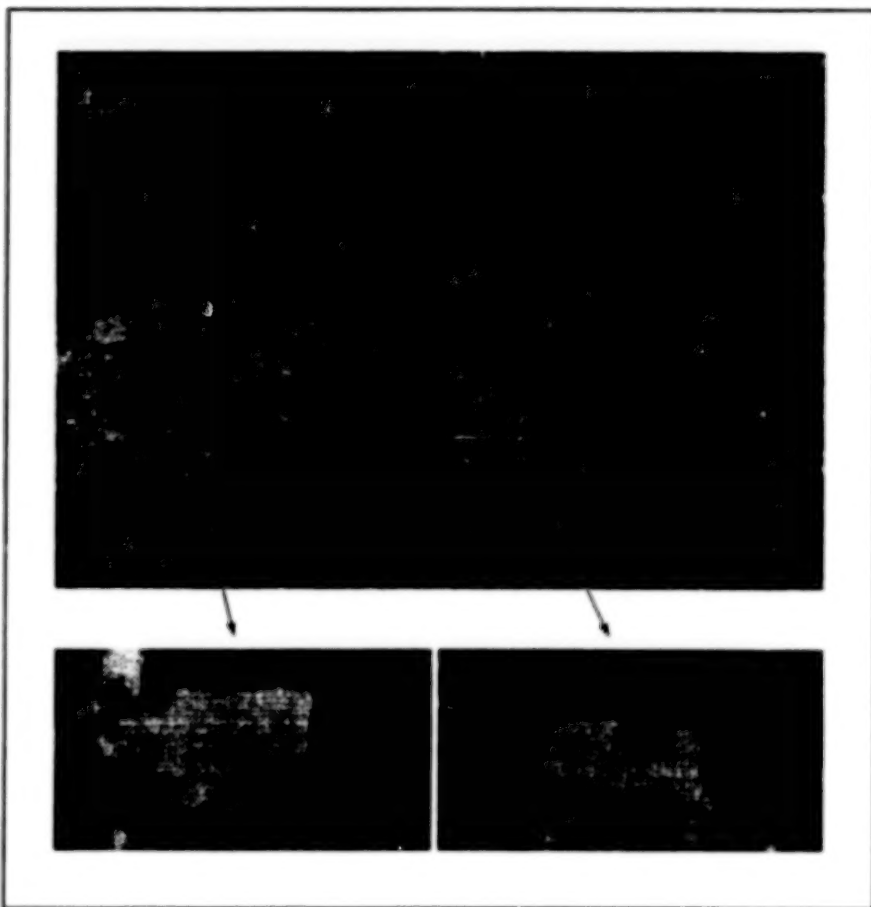
NASA's Jet Propulsion Laboratory,
Pasadena, California

Algorithms have been developed to enable a robotic vision system to recognize, in real time (at a rate between 0.5 and 2 frames per second), known objects lying on the ground. In the original intended application, the algorithms would be executed by off-the-shelf computer hardware aboard a robotic vehicle that would traverse military ordnance-testing ranges to search for unexploded bombs. A stereoscopic pair of color video cameras aboard the vehicle would acquire images of the terrain near the vehicle, and the algorithms would process the digitized images to recognize the bombs by their known size, shape, and color. The algorithms may also be adaptable to other, similar robotic-vision applications — for example, automated recognition of color traffic signs for alerting drivers in automobiles.

The methodology implemented by the algorithms can be summarized as follows: First, raw data from a pair of color stereoscopic images are subjected to rapid preliminary processing to detect candidate locations (that is, locations to be examined more thoroughly for the presence of bombs). Once the candidates have been detected, additional computations are performed to reduce false alarms, reason about the remaining available image data, and make a final decision about each candidate.

The preliminary processing includes several steps that result in the generation of range data from the disparity between the left and right images of the stereoscopic pair. The stereoscopic range data are used initially, along with other abstracted data, to place bounds on the sizes of objects in the scene; this makes it possible to eliminate, from further consideration, all parts of the scene that do not contain candidate objects within the size range of the objects of interest (the bombs in the original application). This elimination reduces the search space and reduces the incidence of false alarms.

Next, the color of each pixel in the remaining search space is quantified by computing a unit vector in a three-axis color space from its red, green, and blue brightnesses. Each pixel is then classified as either like or unlike an object of interest, depending on whether its unit color vector does or does not lie within that volume in the color space that represents the range



Candidate Objects are identified in an image, then resampled to a canonical size and orientation for further processing.

of anticipated variation of color of the object of interest, given anticipated variations in lighting, viewing angles, and natural degradation from weathering. Candidate objects are identified by locating blocks of contiguous pixels that have been so classified.

After detecting candidate locations, a variety of verification software modules can be applied to reduce false alarms. Although verification is more computation-intensive than are the preceding steps, the verification process does not greatly increase the overall computation time because much of the image has been eliminated from consideration in the preceding steps.

The first step in the verification process is to compute the dominant orientation of the object at each candidate location, then use the resulting information, along with the range data, to resample the candidate object at a canonical scale and orientation (see figure). Each resampled candidate object is then subjected to a series of tests

that rate the spatial distribution of color, the likelihood that edges consistent with those of the objects of interest are present, the height of the candidate object, and the contrast between the object and the background. Weighted sums of the quantitative results of these tests are used to compute the probability that the candidate object is one of the objects of interest; the candidate is deemed to be an object of interest if the computed probability exceeds a predetermined threshold value.

The algorithms were tested on 350 images acquired at a live-fire test range near Nellis Air Force base. (Training for the candidate-detection stages was performed on a set of images collected at the same site one year earlier.) Overall, 324 instances of 75 different bombs of the same type appear in the test set. Each bomb was detected in at least one of the images that showed it. Several false negatives occurred in instances in which the

bombs lay at significant distances from the cameras and thus yielded small images. In these cases, the bombs were always detected when the cameras traveled closer to them. In addition, 19 false

alarms were detected. Of the candidate objects reported, 92.6 percent were found to be bombs.

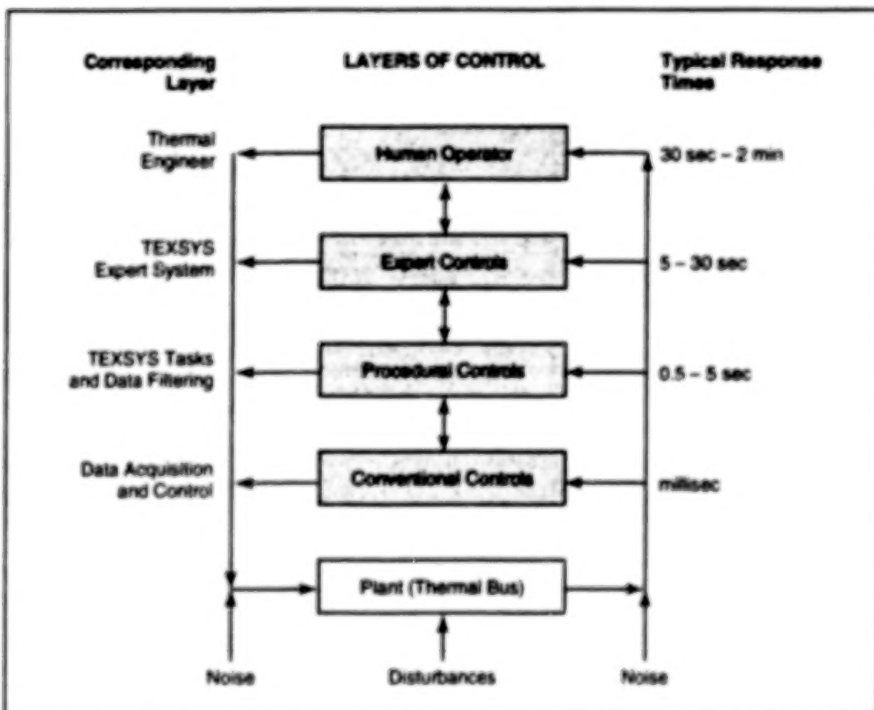
This work was done by Clark F. Olson of Caltech for NASA's Jet Propulsion

Laboratory. Further information is contained in a TSP [see page 1].
NPO-20754

Expert System Controls and Monitors Thermal System

A symbolic controller recognizes malfunctions and takes corrective action.

Ames Research Center,
Moffett Field, California



The Symbolic Control Hierarchy Extends from the hardware layer to the expert system at the top. The hardware is a thermal regulatory system (Carot refrigerator).

The Thermal Expert System (TEXSYS) computer program exerts real-time control over a complicated thermal-regulatory system that includes evaporators, condensers, a pump, valves, and sensors. TEXSYS observes differences between actual and expected conditions and analyzes differences to determine whether a given condition signifies a malfunction in a component or at the system level. It then takes corrective action (e.g., it commands the opening or closing of a valve).

A knowledge base of engineering expertise on the particular thermal-regulatory system is contained in an expert-system computer program called "core TEXSYS." TEXSYS was developed by adding core TEXSYS to conventional software for acquisition of data and for control, forming a hierarchical symbolic controller. The architecture of TEXSYS is layered, with the

expert system at the top, the controlled hardware and conventional controlling hardware and software at the lowest two levels, and an intermediate layer that integrates the expert system with the lower levels (see figure).

The thermal regulatory system to be controlled includes a thermal bus that functions as a Carnot refrigerator, using anhydrous ammonia as the working fluid. A heat-acquisition branch absorbs heat from an external source, changing the working fluid from liquid to mixed liquid and vapor. The mixture is separated in a heat-transport branch by a centrifugal pump, which sends vapor to condensers in a heat-rejection branch and liquid back to the heat-acquisition branch. A regulating valve on the downstream vapor line maintains a constant set-point pressure (and constant temperature, if the

vapor is saturated), much like a relief valve. Once in normal operation, the thermal bus tends to balance itself, requiring control of the valve setting, pump power, and occasionally, the set point.

Real-time control requires response times of tens of seconds — 15 seconds during startup. To ensure fast response, data to be processed by TEXSYS are filtered so that only data on significant changes are entered; steady or slowly changing data, which would take an inordinate amount of time to consider, are eliminated. TEXSYS can identify all of the 7 known system-level faults and the 10 of 34 component-level faults that were chosen by thermal engineers as most interesting or representative.

So that TEXSYS can accept changes in hardware, a library of behaviors of generic components (how valves, pipes, and pumps function) was incorporated and separated from information on the behavior of the specific thermal bus. When thermal bus hardware changes, a new mathematical model is created in TEXSYS by choosing components from this library and connecting them as in the schematic diagram of the hardware. New data from the intermediate or integration layer of TEXSYS are placed into the model at sensor locations, then processed both by active values (across connections) and by rules (across components). The insertion of a datum at a given location in the model may then result in a chain of inferences about the behavior of the system.

This work was done by W. Erickson, B. J. Glass, R. Owens, and M. S. Rudokas of Ames Research Center, R. Levinson of Recom Software, Inc., and J. Nienart of Sterling Software. Further information is contained in a TSP [see page 1].

Inquiries concerning rights for the commercial use of this invention should be addressed to the Patent Counsel, Ames Research Center [see page 10]. Refer to ARC-13166.

Cascade Error-Projection Learning in Neural Networks

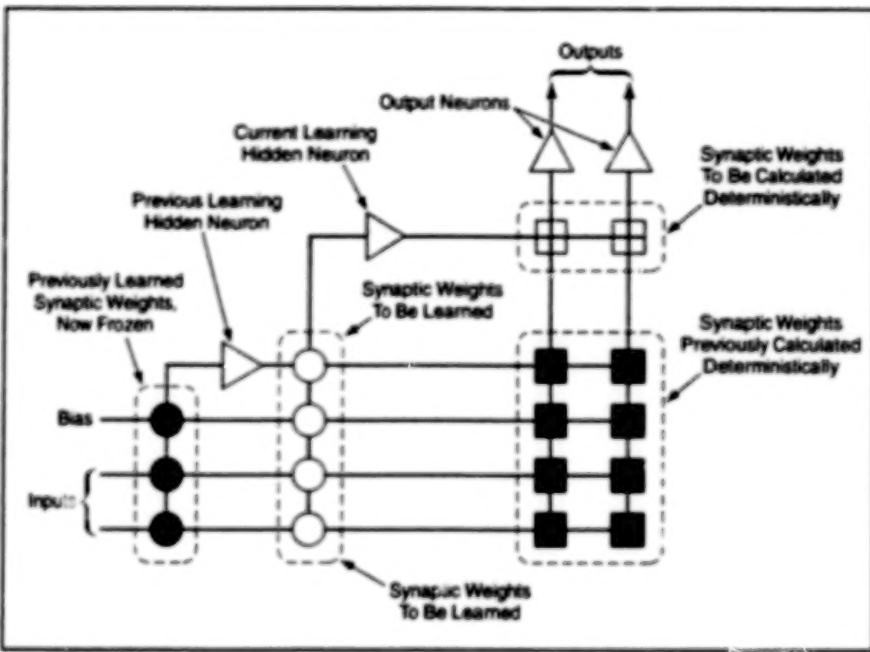
This algorithm involves fewer iterations and can be implemented in simpler hardware.

NASA's Jet Propulsion Laboratory,
Pasadena, California

Cascade error projection (CEP) is an improved learning algorithm for artificial neural networks. CEP is reliable and suitable for efficient implementation in very-large-scale integrated (VLSI) circuitry. In comparison with other neural-network-learning algorithms, CEP involves fewer iterations and is more tolerant of low resolution in the quantization of synaptic weights; thus, CEP learns relatively quickly and the circuitry needed to implement it is relatively simple.

CEP incorporates a cascading-architecture feature (see figure 8) of a prior algorithm called "cascade correlation." CEP also incorporates an independent-learning-neural-layer feature from cascade back-propagation.

In addition, CEP is built on a firm theoretical foundation that involves mathematical modeling of the learning process in terms of the abstract space of synaptic-connection weights. The "projection" aspect of CEP denotes an approach in which an error surface is projected onto the current hidden learning neuron and its synapses. The firm theoretical foundation is provided by a theorem that says, in essence, that as the learning hidden neural units are incorporated into the neural network sequentially in cascade, the resulting cascade of sequential sub-



The Architecture of Cascade Error Propagation includes inputs, hidden neurons, and output neurons. The blank circles represent synaptic weights that are to be learned according to a perceptron approach, while the blank squares represent synaptic weights to be calculated deterministically. The shaded circles and squares represent synaptic weights that have been learned and calculated previously and are now frozen.

spaces ensures that the neural network converges on its learning objective.

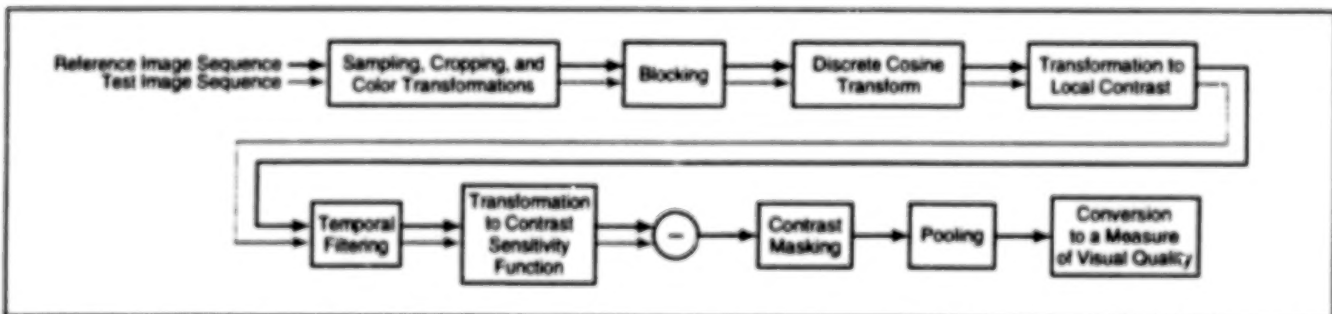
This work was done by Tuan A. Duong of Caltech for NASA's Jet Propulsion

Laboratory. Further information is contained in a TSP [see page 1].
NPO-19644

A Metric for Visual Quality of Digital Video

This metric is based partly on human visual processing and is computationally efficient.

Ames Research Center,
Moffett Field, California



Test and Reference Sequences of digitized video images are processed to generate a measure of the visual quality of the test sequence relative to the reference sequence.

DVO (which stands for "digital video quality") is a metric for evaluating the visual quality of digitized video images. Other video-quality metrics have been proposed, but it appears that each of them (1) may

be based on mathematical models that are not related closely enough to the characteristics of human perception, in which case it may not measure visual quality accurately; or (2) may entail such large

amounts of memory or computation that the contexts in which it can be applied are restricted. In contrast, DVO was developed in an effort to incorporate mathematical models of human visual processing

while maintaining computational efficiency so that accurate metrics can be computed in real time by use of modest computational resources.

DVQ incorporates aspects of early visual processing, including dynamic adaptation to changing brightness, luminance and chromatic channels, spatial and temporal filtering, spatial-frequency channels, dynamic contrast masking, and summation of probabilities. Among the most complex and time-consuming elements of other proposed metrics are spatial-filtering operations that implement multiple-bandpass spatial filters characteristic of human vision. In DVQ, spatial filtering is accelerated by use of the discrete cosine transform (DCT); this provision affords a powerful advantage because efficient computational hardware and software for the DCT are available and because in many potential applications, DCTs may have already been generated in image-data-compression processing.

DVQ is defined by, and computed in, the process illustrated in the figure. The input to the process is a pair of color video image sequences, of which one is denoted the

reference sequence and the other is denoted the test sequence. The first step of the process consists of various sampling, cropping, and color transformations that serve to restrict processing to a region of interest and to represent colors in the sequences in a perceptual color space [e.g., in terms of L (a standard measure of brightness) and chromaticity coordinates (standard measures of hue and saturation) specified by the Commission Internationale de l'Eclairage (CIE)].

The sequences are then subjected to blocking and DCT, the results of which are transformed to local contrast (the ratio between the DCT amplitude and the mean amplitude in the affected block). The next step is a temporal-filtering operation, in which the temporal part of a contrast-sensitivity function (CSF) is implemented in a recursive discrete second-order filter. The outputs from the temporal-filtering operation are converted to just-noticeable differences by dividing each DCT coefficient by its respective visual threshold; this implements the spatial part of the CSF.

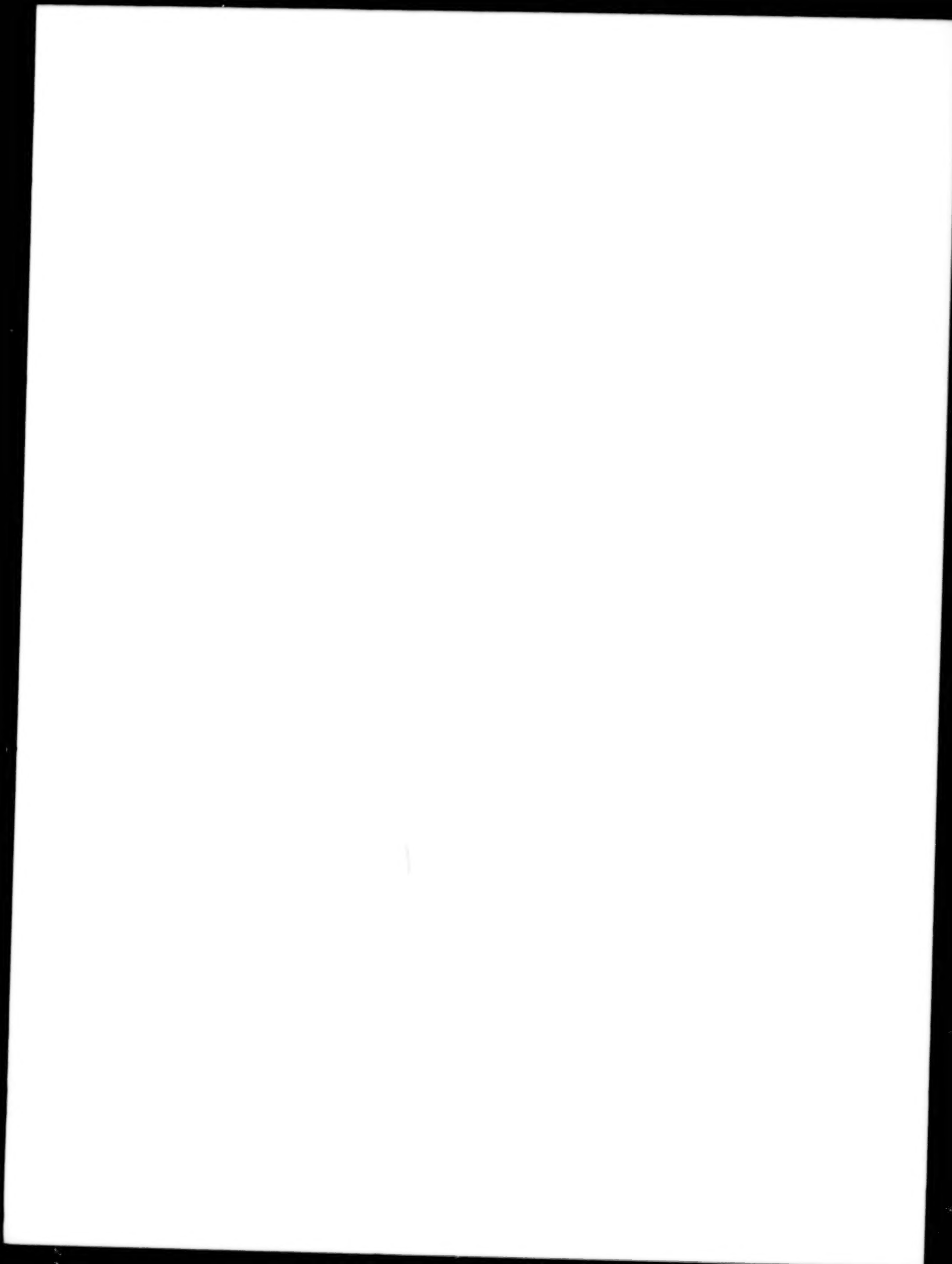
In the next step, the two sequences are subtracted. The resulting difference

sequence is subjected to a contrast-masking operation, which also depends upon the reference sequence.

Finally, the masked differences can be pooled in various ways to illustrate the perceptual error over various dimensions. As used here, "pooling" signifies summing over one or more of six dimensions that represent, specifically, image frames, color channels, rows of blocks, columns of blocks, horizontal spatial frequencies, and vertical spatial frequencies. The pooled error can be converted to a measure of visual quality.

This work was done by Andrew B. Watson, James Hu, and John F. McGowan III of Ames Research Center. Further information is contained in a TSP [see page 1].

This invention is owned by NASA, and a patent application has been filed. Inquiries concerning nonexclusive or exclusive license for its commercial development should be addressed to the Patent Counsel, Ames Research Center, (650) 604-5104. Refer to ARC-14236.



END

12-4-01